Catalytic Activity of AuCu Clusters on MgO(100): Effect of Alloy Composition for CO Oxidation

Li Ma,[†,‡] Kari Laasonen,[§] and Jaakko Akola*[,†,‡,¶]

[†]Department of Physics, Tampere University of Technology, FI-33101 Tampere, Finland

[‡]COMP Centre of Excellence, Department of Applied Physics, Aalto University, FI-00076 Aalto, Finland

[§]COMP Centre of Excellence, Department of Chemistry, Aalto University, FI-00076 Aalto, Finland

[¶]Department of Physics, Norwegian University of Science and Technology, NO-7491, Trondheim, Norway

ABSTRACT

Density functional simulations have been performed for Au_7Cu_{23} and $Au_{23}Cu_7$ clusters on MgO(100) supports to probe their catalytic activity for CO oxidation. The adsorption of reactants, O_2 and CO, and potential O_2 dissociation have been investigated in detail by tuning the location of vacancies (F-center, V-center) in MgO(100). The total charge on Au_7Cu_{23} and $Au_{23}Cu_7$ is negative on all supports, regardless of the presence of vacancies, but the effect is significantly amplified on the F-center. Au_7Cu_{23}/MgO(100) and $Au_{23}Cu_7$/MgO(100) with an F-center are the only systems to bind O_2 more strongly than CO. In each case, O_2 can be effectively activated upon adsorption and dissociated to 2×O atoms, in particular on the F-center. The different reaction paths based on the Langmuir−Hinshelwood (LH) and Eley−Rideal (ER) mechanisms for CO oxidation have been explored on the Au_7Cu_{23} and $Au_{23}Cu_7$ clusters on F-centers, and the results are compared with the previous findings for $Au_{15}Cu_{15}$. Overall, the reaction barriers are small, but the changes in the Au:Cu ratio tune the reactant adsorption energies and sites considerably showing also varying selectivity for CO and O_2. The microkinetic model built on the basis of the above results shows a pronounced CO_2 production rate at low temperature for the clusters on F-centers.

1. INTRODUCTION

Bimetallic clusters have caught considerable attention over the past decade, since they provide the possibility to tailor the size and the composition of nanocatalyst systems. The synergetic effects between different metals can eventually result in a material with enhanced catalytic properties.[1-6] Generally, the synergy arises from interactions among metals, which can modify the electronic or structural properties of the active sites.

Gold nanoparticles supported on metal oxides have been proven to be highly active and selective catalysts for a variety of chemical reactions.[7] One of the most notable example is the reaction of CO oxidation at low temperature.[8-10] However, most Au catalysts still suffer from rapid deactivation, which is a drawback for practical applications. The deactivation mechanism is often attributed to the sintering of Au particles.[11,12] Correspondingly, it is challenging to prepare small gold nanoparticles on inert supports (*e.g.*, SiO_2, Al_2O_3, MgO) without anchoring sites (*e.g.*, defects, F-centers). It has been also reported that the F-center on MgO surface plays a critical role in the activation of Au catalysts.[13,14] High catalytic activity for clusters with more than 8 gold atoms has been demonstrated by experiments for the CO oxidation on selected Au_n clusters deposited on defect-rich MgO(100) films at low temperatures.[13] The adsorption and activation of O_2 are important steps in the CO oxidation reaction,[15] and the oxide support is supposed to affect the activation of oxygen.[16,17] The catalytic activity of Au nanoparticles is significantly reduced on inert substrates, which cannot facilitate strong adsorption for O_2 molecules and result in high O_2 dissociation barriers. Here, alloying with a second metal is an effective way to improve the capability of Au to activate molecular oxygen, and, for example, Cu can play such a role.[18] Catalysts based on Au−Cu alloys have been reported as promising and effective catalysts for low temperature CO oxidation because of the synergistic interaction between Cu and Au.[19,20] They exhibit higher activity and resistance against sintering in comparison to monometallic Au catalysts.

In practice, a number of factors influence the catalytic performance of bimetallic nanoparticles, *e.g*., nanostructure, composition, size, and the chemical structure of the support (including defects). Thus, the catalytic process is a complex problem. Concerning nanoparticle composition, there is controversy of the effect of the Au/Cu ratio for the activity towards CO oxidation. Mozer *et al.*[21] found a correlation between activity and Cu loading of an alumina-supported Au catalyst. While low amounts of copper were beneficial for the CO oxidation activity, high copper contents caused blocking of the Au active sites, thus decreasing the catalytic activity. However, Sandoval *et al.*[20] reported the highest activity of CO oxidation for AuCu/TiO_2 catalyst with a somewhat higher Au:Cu ratio of 1:0.9. Moreover, the effect of redox treatments on AuCu nanoparticles is also a matter of controversy in experimental studies.[22-24]

AuCu systems have three ordered alloys in the bulk: $Au_{0.5}Cu_{0.5}$ (fcc, L_{10}), $Au_{0.25}Cu_{0.75}$ (fcc, L_{12}) and $Au_{0.75}Cu_{0.25}$ (fcc, L_{12}), and experiments have shown that the stoichiometry of bulk alloys can be reproduced well also in AuCu clusters.[25] Pauwels *et al.*[26] reported AuCu clusters generated by laser vaporization and deposited at low kinetic energy on MgO substrate. The clusters were observed to adopt the truncated octahedral morphology. In particular, the clusters with the stoichiometric compositions $Au_{0.25}Cu_{0.75}$, $Au_{0.5}Cu_{0.5}$ and $Au_{0.75}Cu_{0.25}$ were all found to have an fcc structure and to be in a cube-on-cube epitaxy relation with MgO(100).

To explore the catalytic activity of AuCu clusters, we have previously performed a systematic study of $Au_{15}Cu_{15}$ (1:1 composition) on MgO(100) with and without vacancies for CO oxidation.[27] Our calculations revealed that O_2 can be effectively activated upon adsorption and dissociated to 2×O atoms easily. The reaction barriers were systematically lower for the substrate with an F-center. Here, we aim to investigate how the cluster composition itself affects these results, and we concentrate on two AuCu clusters (1:3 and 3:1) with the same size and pyramidal shape (fcc). As shown by Ferrando *et al.* by using the global optimization search and density functional theory (DFT) calculations,[28] the fcc pyramidal structure is energetically favorable for 30-atom AuCu

clusters on MgO(100). Here, we use DFT combined with a microkinetic model to elucidate the CO oxidation reaction mechanism on the MgO-supported Au_7Cu_{23} and $Au_{23}Cu_7$ clusters and demonstrate the effect of the Au/Cu ratio and the role of vacancies in the MgO(100) support. Although the associated formation energies are high, experimental studies have shown that the vacancies or defect sites exist on the MgO(100) single crystal surface,[29-33] which is either cleaved or grown on a metal support in ultrahigh vacuum. Furthermore, such defect sites can be generated by Ar sputtering, and they have been generally considered as the main anchoring sites in the nucleation and growth of metal particles or thin films.[29,34,35] Previously, many experimental and theoretical studies have been devoted to single metal/MgO(100) systems.[29,36-42] The key issues to understand have been how metal adatoms adsorb and grow on the surface and how this couples to the properties of the metal-oxide interface and the MgO(100) surface itself.

2. COMPUTATIONAL METHOD

The DFT calculations were performed using the CP2K program package.[43,44] The exchange-correlation interaction was treated within the spin-polarized generalized gradient approximation with the functional form by Perdew-Burke-Ernzerhof (GGA-PBE).[45] Gaussian and plane wave (GPW) basis sets were used to represent the Kohn-Sham orbitals and electron density. A molecularly-optimized double-zeta valence plus polarization (DZVP) basis set[46] was used for the Gaussian expansion of the wave functions. Herein, the basis set superposition error (BSSE) has been reduced during the basis set optimization. The complementary plane wave basis set has a 600 Ry energy cutoff for the calculation steps involving electron density. The description of the valence electron-ion interaction is based on the analytic pseudopotentials derived by Goedecker, Teter, and Hutter (GTH).[47]

The MgO(100) substrate was modeled by a four-layer slab with 36 Mg and 36 O atoms in each layer (in total 288 atoms) and a vacuum layer of 20 Å. It has been previously shown that the

relaxation of substrate atoms has very small effects during the optimization.[28,48] The lower two layers of the substrate were held frozen at the optimal DFT lattice constant of 4.24 Å (experimental value 4.22 Å).[48] The previously published[26,28] fcc pyramidal geometries of Au_7Cu_{23} and $Au_{23}Cu_7$ clusters were chosen as the model structures on MgO(100). To illustrate the effect of support vacancies, three cases were considered: an ideal MgO support (defect-free), MgO support having an O-vacancy (F-center), and MgO support with an Mg-vacancy (V-center). The energetically most favorable adsorption configurations of Au_7Cu_{23} and $Au_{23}Cu_7$ on MgO(100) on vacancies were located by examining the different point defects sites with respect to the AuCu cluster position on MgO(100). The adsorption energies of Au_7Cu_{23} and $Au_{23}Cu_7$ clusters (E_{ad}^1) on MgO(100) supports were computed as:

$$E_{ad}^1 = E(AuCu) + E(MgO) - E(AuCu/MgO) \quad (1)$$

For the molecular and atomic adsorption of reactants on Au_7Cu_{23}/MgO and $Au_{23}Cu_7$/MgO, the adsorption energy (E_{ad}^2) of a given arrangement was computed as:

$$E_{ad}^2 = E(AuCu/MgO) + E(adsorbant) - E(AuCu/MgO + adsorbant) \quad (2)$$

Here, $E(X)$ in Eqs. (1) and (2) is the total energy of the corresponding system X and AuCu refers to Au_7Cu_{23} or $Au_{23}Cu_7$.

We used the Bader method for evaluating the spatial atomic charge decomposition.[49] The reaction pathways were mapped using the climbing image nudged elastic band (CI-NEB) method.[50] The obtained minima and transition states structures were further identified by vibrational analysis. Zero-point energy (ZPE) corrections were systematically included in the energy and reaction barrier calculations. In addition, the hybrid DFT functionals (PBE0 and B3LYP) have been previously tested in our CO oxidation benchmarks on Cu clusters,[51] where we observed that the energetic ordering of different reactions paths (barriers) remained the same although the reaction barriers were systematically lower for GGA-PBE. Furthermore, the different spin states were checked for the MgO(100) substrate with F- and V-center defects. The energy of the singlet state is 1.34 eV

lower than that of the triplet state for the F-center, whereas the triplet state is energetically 0.35 eV lower for the V-center. However, the energy of the singlet state is always lower than that of triplet state once the AuCu clusters have been adsorbed on the substrate.

3. **RESULTS AND DISCUSSION**

3.1. Au_7Cu_{23} and $Au_{23}Cu_7$ on MgO Supports

Figure 1 gives the most stable adsorption geometries of Au_7Cu_{23} and $Au_{23}Cu_7$ on three MgO(100) supports and the corresponding MgO(100) surfaces with assigned point defects sites. The adsorption energy, geometric parameters, and charge transfer between clusters and MgO(100) are listed in Table 1. The corresponding values for $Au_{15}Cu_{15}$/MgO[27] are also included in Table 1 for comparison.

On the defect-free MgO surface (Figure 1), the Au_7Cu_{23} and $Au_{23}Cu_7$ clusters retain the symmetric (C_{2v}) fcc pyramidal structure with Au-O and Cu-O bonds between the AuCu/MgO interface. The Au-Au, Cu-Cu, and Au-Cu bond lengths of Au_7Cu_{23} are in the range of 2.82 Å, 2.44-2.68 Å, and 2.49-2.77 Å, respectively. The corresponding bond lengths of $Au_{23}Cu_7$ are in the range of 2.66-3.19 Å, 2.62-2.91 Å, and 2.63-2.97 Å, respectively. The shape of the bottom layer of the Au_7Cu_{23} cluster is a square with 4 Au atoms on the corners and 12 Cu atoms on the center and periphery. Upon adsorption, the Cu atoms directly above support O atoms move down forming Cu-O bonds in the range of 2.11-2.43 Å, which are considerably shorter than the Au-O bonds (2.79-2.93 Å). For the square bottom layer of the $Au_{23}Cu_7$ cluster, 2 Cu atoms locate on the center forming Cu-O bonds of 2.21 Å, compared with the 14 Au-O bonds in the range of 2.59-2.76 Å. Bader charge analysis shows that Au_7Cu_{23} and $Au_{23}Cu_7$ carry a net charge of -1.96 e and -2.15 e, respectively, which indicates that MgO(100) has transferred charge (electrons) to the cluster. A detailed analysis of the atomic charges in Au_7Cu_{23} shows that Au atoms gain electron density up to

0.60 e, while Cu atoms lose electron density up to 0.20 e. Similarly, for the $Au_{23}Cu_7$ cluster, Au atoms gain electron density up to 0.42 e while Cu atoms lose electron density up to 0.38 e.

For the F-center support, the geometries of Au_7Cu_{23} and $Au_{23}Cu_7$ change primarily by the downward movement of the corner Au atom towards the F-center (C_s) (Figure 1). The adsorption energies of Au_7Cu_{23} and $Au_{23}Cu_7$ increase to 6.35 eV and 7.06 eV, and the clusters are pronouncedly negatively charged by total charges of -3.41 e and -3.66 e, respectively. The Au atom above the F-center in Au_7Cu_{23} is strongly negatively charged by -1.53 e, which considerably differs from the defect-free case (-0.58 e). The other Au atoms are negatively charged down to -0.63 e, while all Cu atoms are positively charged up to +0.20 e. Similarly, the Au atom above the F-center in $Au_{23}Cu_7$ is negatively charged by -1.20 e compared to the -0.24 e in the defect-free case. The charge transfer from the F-center has both local and nonlocal components as approximately one half of the charge transferred locates in the pointing Au atom and the rest is mainly distributed across the other Au atoms.

For the V-center, the defect locates below the center of the bottom layer of Au_7Cu_{23} and $Au_{23}Cu_7$ (Figure 1, C_{2v} symmetry). The binding energies of Au_7Cu_{23}/MgO and $Au_{23}Cu_7$/MgO are the highest (9.55 and 7.78 eV) of all supports. Here, the triplet state was used for the V-center alone to take into account the correct spin state. The strong adsorption causes that the Au-O and Cu-O bond lengths decrease for both cases, while the charge transfer from the support is the smallest (Table 1). Such interaction with the support is advantageous because pinned AuCu clusters are less susceptible to deactivation due to thermal sintering. As analyzed for $Au_{15}Cu_{15}$/MgO(100),[27] there is no direct relationship between the interaction energy and the charge transfer for AuCu/MgO systems. The amount of charge transfer relates to the electronic nature of defects, where the F-center stands out due to its two hosted electrons. In general, the larger electron negativity of Au (2.4 compared to 1.9 of Cu)[52] yields that Au atoms are negatively charged, while Cu atoms are positively charged.

3.2. O_2 and CO Adsorption Energies

Previously, it has been found for CO oxidation on free and supported Au clusters that the strong CO binding on Au hinders the adsorption of O_2,[53,54] leading to CO poisoning and a low reaction rate. In the case of the $Au_{15}Cu_{15}$/MgO model catalyst we also confirmed that the cluster preferentially binds CO over O_2.[27] However, the Au_7Cu_3/CeO_2 system has been reported to bind O_2 more strongly than CO.[55] Here, we examine all individual adsorption sites of Au_7Cu_{23} and $Au_{23}Cu_7$ on MgO supports for O_2 and CO adsorption.

Table 2 shows the energies (E_{ad}^2) of O_2 and CO binding on Au_7Cu_{23} and $Au_{23}Cu_7$ with MgO supports. The adsorption energy of O_2 is less than 0.01 eV for the $Au_{23}Cu_7$/MgO system with V-center indicating no binding for oxygen molecule (missing row). The most stable adsorption configurations are given in Figure S1. The O_2 molecules have similar adsorption configurations on Au_7Cu_{23}/MgO and $Au_{23}Cu_7$/MgO, where the molecule is rotated on the bridge site of a Cu-Cu and Au-Au bond, respectively, at the interface between the cluster and support. These differ considerably from the adsorption on $Au_{15}Cu_{15}$/MgO,[27] where a Cu-Cu bond on the cluster facet is the preferable adsorption site (bridge site). The direct interaction with the substrate causes that the charge transfer to O_2 from Au_7Cu_{23}/MgO (1.11e – 1.46e) and $Au_{23}Cu_7$/MgO (0.89e – 1.18e) is more than that of $Au_{15}Cu_{15}$/MgO (0.68e – 0.84e). For the CO molecule, the preferable binding sites involve Cu atoms on the cluster facet in each case (hollow, bridge and top sites). The binding energy of CO is similar or stronger than that of O_2 on the defect-free and V-center Au_7Cu_{23}/MgO(100) systems (Table 2). The defect-free $Au_{23}Cu_7$/MgO(100) system binds also CO more strongly than O_2. This means that CO poisoning is a likely phenomenon for these catalysts. However, the clusters on the F-center prefer clearly to bind O_2. Typically, it is considered that the molecule with the larger adsorption energy is likely to pre-adsorb on the catalyst. Therefore, the Au_7Cu_{23} and $Au_{23}Cu_7$ clusters on the F-center support appear promising catalysts for CO oxidation.

To further understand the electronic structure upon O_2 adsorption, Figure 2 gives the projected density of states (PDOS) of Au_7Cu_{23} and $Au_{23}Cu_7$ on the F-center with an adsorbed O_2 molecule.

The HOMO and LUMO states of the gas phase triplet O_2 molecule are also included for reference, and these are two-fold degenerate, each. Upon adsorption of O_2, an electron is transferred to the empty $2\pi^*$ orbitals (LUMO) which is pulled down below the Fermi energy. This results in elongation of the O-O bond [1.51 Å and 1.47 Å (Table 2) versus 1.24 Å for the gas phase] and the molecule is activated to the superoxo O_2^- state. Interestingly, the electronic states involving oxygen are exactly at the valence band edge in $Au_{23}Cu_7$, while those for Au_7Cu_{23} are shifted farther below the Fermi energy. There is no spin polarization for systems with O_2 adsorption, which is different from our previous studies for the Cu_{20} cluster, where electron density is transferred from the Cu cluster to O_2 causing local spin-polarization.[51]

The visualizations of the charge density differences (CDD) and the HOMO and LUMO states for the O_2 adsorption are displayed in Figure 3. Combined with the information in Figures 2 and 3, one can see the strong charge transfer for O_2 and that the bonding at the cluster-support interface is due to the hybridization of the oxygen *p* states (from the molecule and MgO support) and *d* states of Au and Cu (see also Figures S2 and S3). The HOMO orbital of the $Au_{23}Cu_7$ system displays significant contribution on O_2, as suggested based on PDOS, but the orbital is not completely localized. In addition, the *d*-band center (C_d) has been calculated to discern the difference in these two systems. The C_d values are -2.45 eV and -3.16 eV, respectively, for the O_2 adsorbed Au_7Cu_{23} and $Au_{23}Cu_7$ on the F-center (the corresponding value for $Au_{15}Cu_{15}$ is -2.89 eV, Ref. 27). Au_7Cu_{23} pushes the *d*-band center higher than $Au_{23}Cu_7$ due to the stronger binding with O_2 and more charge (electron) transfer towards the molecule.

3.3. O_2 Dissociation

As mentioned above, the adsorption and activation of O_2 molecules are important steps in the CO oxidation reaction. It is known that O_2 cannot dissociate on Au since it exhibits large dissociation energy barriers.[17,56,57] However, recent experimental and computational studies have shown that O_2 can adsorb dissociatively on Cu clusters.[51,58] Moreover, the O_2 molecule can be effectively activated

upon adsorption and dissociated to 2×O atoms easily on $Au_{15}Cu_{15}$/MgO(100).[27] Thus, we investigated the dissociation of O_2 on the most stable binding geometries of Au_7Cu_{23}/MgO(100) and $Au_{23}Cu_7$/MgO(100) with or without defects before examining the CO oxidation mechanisms. For the O_2 dissociative adsorption, the total energy of oxygen molecule (triplet state) was used as *E(adsorbate)* in Eq. 2 to take into account the correct spin state of the gas phase O_2.

The identified lowest-energy reaction paths for the O-O bond cleavage on Au_7Cu_{23} and $Au_{23}Cu_7$ with the F-center supports are shown in Figure 4. For the defect-free and V-center supports, the corresponding reaction paths are given in Figure S4. The adsorption energy (E_{ad}^2) of the dissociated O_2 (2×O), bond length of O_2 (r_{O-O}), charge transfer (Q) to O_2 and 2×O, and activation energy barriers ($O_2 \rightarrow O + O$) for the most stable adsorption complex are listed in Table 2.

The adsorption energies of O_2 and 2×O are higher on Au_7Cu_{23}/MgO(100) than those on $Au_{23}Cu_7$/MgO(100), which clearly correlates with the Cu content. The preferred adsorption patterns of 2×O are hollow sites on Au_7Cu_{23}/MgO(100) and $Au_{23}Cu_7$/MgO(100) with different supports (Figures 4 and S4). In each case, one oxygen atom binds between the cluster and the substrate interface, whereas there is variation with the location of the other one on the cluster facet. The dissociative adsorption is energetically preferred with more charge transfer (Table 2). Similar to the O_2 case, the substrate affects the charge of the adsorbed oxygen atom at the interface.

For Au_7Cu_{23}/MgO(100), the O_2 and 2×O adsorption energies are highest on the F-center and lowest on the V-center support. The calculated dissociative reaction barriers are very small on all supported clusters, but in particularly on the F-center (0.13 eV). For $Au_{23}Cu_7$/MgO(100), the O_2 adsorption energy is higher on the F-center, while the values are nearly the same for the 2×O adsorption. The energy barrier is 0.62 eV for O_2 dissociation on F-center support. Although the barriers are higher than those on Au_7Cu_{23}/MgO and $Au_{15}Cu_{15}$/MgO (0.15 eV),[27] they are still lower than the dissociation on Au catalysts (more than 1.0 eV).[17] Obviously, alloying Au with Cu increases the binding of O_2 and benefits the molecular dissociation.

3.4. Reaction Mechanisms for CO Oxidation

The clusters on the F-center are the only systems which clearly prefer to bind O_2 more strongly than CO, and they also dissociate O_2 molecule readily. Therefore, these two systems are selected for a further study on CO oxidation. Both the Langmuir-Hinshelwood (LH) and Eley-Rideal (ER) mechanisms are considered,[59] and the reaction paths with dissociated O atoms are also taken into account. The results of the reaction paths and energetics are displayed in Figures 5-7 and S5-S6.

The LH reaction mechanism is initiated by the co-adsorption of O_2 and CO. The catalytic reaction pathways are shown in Figure 5 for the lowest energy co-adsorption configurations on the Au_7Cu_{23}/MgO(100) system with F-center. To compare the energies easily, the activation and reaction energies of different reaction pathways are summarized in Table 3. For O_2* + CO*, the preferable co-adsorption pattern involves the bottom Cu−Cu site for O_2 and the hollow (three Cu atoms) site for CO on Au_7Cu_{23}. The co-adsorption energy is 3.09 eV (Table S1), which is comparable to the sum of single O_2 and CO adsorption energies (3.16 eV) on the same system. The O-O and C=O bond lengths are not affected by the co-adsorption (Table S1). After the initial adsorption, the LH reaction proceeds via a barrier (TS) of 0.21 eV to a metastable intermediate (IM) state. The O-O and C=O bonds are slightly elongated to 1.54 Å and 1.21 Å in the IM state. Subsequent to the IM complex, there is a barrierless release of the formed CO_2 molecule. Co-adsorption of another CO at the closest bridge site with the remaining O atom (O* + CO*) leads to the formation of second CO_2 with a barrier (TS) of 0.52 eV (middle row). An IM state with weak bonding (0.08 eV) of CO_2 is formed also in this reaction. The catalytic cycle is completed after this step. Alternatively, the first CO_2 formation may involve a reaction with the pre-dissociated O_2. Upon the co-adsorption of 2×O* + CO* (bottom row), CO and the nearest O move closer to each other, followed by a crossing of the energy barrier (TS) to form the IM complex with an activation energy of 0.35 eV. After that a CO_2 molecule is released. The rest of the catalytic cycle repeats the step with a single oxygen, *i.e*. O* + CO* ↔ CO_2.

The ER mechanism involves an attack of a gaseous CO molecule on a pre-adsorbed O_2 or 2×O on Au_7Cu_{23}/MgO(100) with F-center. The role of the catalyst is determined mainly by its effect on O_2. The reaction pathways and the calculated activation barriers are displayed in Figure S5 and Table 3. The abstraction of first O atom from O_2 molecule needs to overcome a very small energy barrier of 0.14 eV and the O–O bond is already broken in the TS, which stems from the high-degree activation of O_2 upon adsorption on Au_7Cu_{23}. The activation energy barrier of TS increases to 0.29 eV for the abstraction of second O atom. For the 2×O* + CO reaction, the TS barrier is 0.31 eV for the first CO_2 molecule release.

For the $Au_{23}Cu_7$/MgO(100) system with F-center, similar reaction steps are considered. Figure 6 displays the LH reaction pathways. The values of the activation barriers are also included in Table 3. In this case, CO adsorbs on the top Cu site, and O_2 binds to the bottom Au−Au site. The co-adsorption energy of O_2* + CO* is higher than the sum of the single O_2 and CO adsorption energies by 0.40 eV (Table S1), which means that the co-adsorption system is energetically lower than those of the individual adsorbates. Upon the co-adsorption of CO and O_2, the molecules move closer to each other, followed by the breaking of O-O bond with the activation energy barrier (TS) of 0.27 eV to form the first CO_2 molecule. After the first CO_2 molecule release, the co-adsorption of a new CO molecule leads to formation of another CO_2 with a barrier of 0.77 eV (middle row). The resulting CO_2 gets effectively ejected out from the cluster. After this step, the catalytic cycle for CO* + O_2* is completed. For the dissociated O_2 (bottom row), CO adsorbs on the top Au site and the corresponding TS has an activation energy of 0.53 eV. The process continues as described for a single oxygen atom (middle row).

Figure S6 displays the ER reaction pathways and the corresponding energy barriers are also listed in Table 3. The abstraction of the first oxygen atom in the reaction O_2* + CO needs to overcome an energy barrier of 0.30 eV. The O_2 bond length is elongated to 1.67 Å in TS while the C=O bond is hardly influenced. The subsequent step is CO oxidation with the remaining O atom. The

corresponding barrier is 0.42 eV. Furthermore, the barrier for the reaction with the dissociated O_2 (2×O* + CO) is 0.29 eV.

The potential energy diagrams of CO oxidation with all the reaction pathways analyzed above are plotted in Figure 7. The corresponding reaction pathways for the $Au_{15}Cu_{15}$/MgO(100) system with F-center are also included for comparison. The exothermic nature of the CO oxidation process is clearly demonstrated with the formation of two CO_2 molecules, and the interesting aspects involve the evolution of reactions in each case. The results show a strong adsorption for the Cu-rich cluster, and the energy deviation among difference reactants decreases with increasing the Au:Cu ratio. For Au_7Cu_{23} and $Au_{15}Cu_{15}$, the adsorption energy of 2O*+CO (ER channel) is lower than O_2*+CO*, while it is the reverse for $Au_{23}Cu_7$. Correspondingly, the dissociation barriers of the O_2 molecule (figure insets) increase as the Au content increases. These results indicate that Cu-rich alloys may exhibit over-binding of reactants (Table S1), and this can block CO oxidation. In particular, Cu is prone to O atoms which is related to its notorious oxidation properties.

Generally, the reaction barriers for CO oxidation are small on the AuCu/MgO systems with the F-center defect. The LH mechanism is lower in energy overall due to the adsorption energies of both CO and O_2 (or 2×O), while the ER mechanism is missing the CO adsorption component. The strong binding of oxygen on Au_7Cu_{23} results in that energy is already rather close to final level after the first CO_2 formation, whereas $Au_{23}Cu_7$ is only halfway through. The CO oxidation barriers on the $Au_{15}Cu_{15}$ cluster are mostly lower than those on the other two systems, especially for the ER reaction pathways. This can be understood further by inspecting the PDOS upon O_2 adsorption (Figure S7) which shows strong weight on oxygen at the Fermi energy and its contribution on both sides of the narrow band gap. This indicates increased reactivity for adsorbed O_2 and explains the low barrier for approaching CO.

The above results show that the AuCu alloys are good catalyst for CO oxidation. However, the choice of the Au:Cu ratio has important consequences for the catalytic activity, which will be

shown more clearly in the microkinetic modelling below. We remark that we have focused here on low O_2 and CO concentrations and we have not studied the effect of several oxygen molecules or oxidation. Higher reactant coverages would require an enormous number of configurations and such computations are out of the content of this study.

3.5. Microkinetic Model

On the basis of the DFT calculations, a 7-step microkinetic model[27,60] was developed to further investigate the activity of the Au_7Cu_{23}/MgO(100) and $Au_{23}Cu_7$/MgO(100) catalysts on F-centers. In comparison to the molecular reaction studied above, the microkinetic model is a simplification, which ignores the two pre-dissociated O* containing reactions and atomistic details of the reactions. However, this model enables us to incorporate real experimental variables, such as partial pressures and temperatures. Moreover, the model complements the DFT calculations by including average surface coverage effects. The elementary steps and full details of the model have been described already in Ref. 27.

Although there is no direct experimental data for CO oxidation on MgO-supported AuCu clusters, CO oxidation on MgO-supported Au clusters has been studied extensively.[13,14] Especially, Yoon[13] *et al.* found that CO_2 was produced at 140 K and 280 K on F-center-rich Au_8/MgO(100) thin films. Moreover, Henkelman *et al.*[55] studied several Au-based bimetallic nanoclusters and found that CeO_2(111)-supported Au_7Cu_3 cluster is optimal for catalyzing CO oxidation, and the microkinetic model clearly indicates a higher activity for the AuCu catalyst under the condition of T = 298 K, $P(CO)$ = 0.01 bar, and $P(O_2)$ = 0.21 bar. Our previous study also shows that $P(CO)$ = 0.01 bar is the most beneficial choice for CO_2 production on the $Au_{15}Cu_{15}$/MgO(100) system with F-center.[27] However, the stronger CO binding on $Au_{15}Cu_{15}$ leads to CO poisoning of the cluster surface for similar partial pressures of CO and O_2. Here, the situation is different as the Au_7Cu_{23}/MgO(100) and $Au_{23}Cu_7$/MgO(100) systems with F-center prefer to bind O_2 more strongly than CO. We use the condition $P(CO)$ = 0.01 bar with different O_2 partial pressures combined with

T = 150K and 300 K in the microkinetic model to evaluate catalyst coverages and the rate of CO_2 formation at longer time scales. The results are collected in Table 4.

Table 4 shows that the rate of CO_2 formation increases significantly with temperature increase from 150 K to 300 K for both systems. Interestingly, at higher O_2 partial pressures, the coverage of O is high, while that of O_2 and CO remains negligible. This can be understood in terms of the DFT calculations where O_2 binding is stronger than that of CO, and O_2 dissociates rather readily to O atoms on these two systems. Moreover, the CO_2 formation is saturated when the O_2 partial pressures is increased. Based on these observations, we chose CO and O_2 with the same partial pressure of 0.01 bar and T = 300 K to investigate further the CO_2 formation on these two systems.

Figure 8 shows the coverages of reactant species (O_2, CO, O) and the turn over frequency (TOF) of CO_2 from microkinetic model simulations as a function of time for Au_7Cu_{23}/MgO(100) and $Au_{23}Cu_7$/MgO(100) at $P(CO)$ = 0.01 bar, $P(O_2)$ = 0.01 bar, and T = 300 K. Throughout the process, the coverage of O remains at a relatively high level, while the coverage of O_2 is negligible for both systems. The O_2 molecules dissociate immediately after adsorption or they are rapidly consumed in the CO oxidation processes. The CO overage is saturated at a moderate level and the steady state is reached with CO_2 production. While the trends for CO_2 production are different for the two cases, the TOF of the CO_2 production is still pronounced for $Au_{23}Cu_7$/MgO(100). On the other hand, high oxygen coverages may cause oxidation of Cu sites in Cu-rich clusters, and redox reactions may also occur during the CO oxidation process.

Finally, we note that the MgO support with the F-center defect is crucial for catalytic activity. As shown in detail for the $Au_{15}Cu_{15}$/MgO system,[27] the rate of CO_2 production is very low on the defect-free or V-center MgO supports. In addition, the Au:Cu ratio influences the reaction conditions and the CO_2 production. For $Au_{15}Cu_{15}$, we observe CO oxidation activity already at 150 K,[27] while there is almost no CO_2 production for Au_7Cu_{23} and $Au_{23}Cu_7$. As the temperature is increased to 300 K, the production of CO_2 increases markedly for all three compositions.

Remarkably, the CO_2 production rate of the $Au_{15}Cu_{15}$ catalyst (~10^7 s^{-1}) is ten times faster than that of Au_7Cu_{23} (~10^6 s^{-1}), while the latter is two orders of magnitude faster than the $Au_{23}Cu_7$ (~10^4 s^{-1}) catalyst. However, the CO_2 production of $Au_{15}Cu_{15}$ is very sensitive to the CO partial pressure as the CO binding energy is higher than that of O_2. For Au_7Cu_{23} and $Au_{23}Cu_7$, the interface adsorption effect leads to the stronger binding of O_2, which modifies the sensitivity of the catalyst to CO and O_2 partial pressures.

4. CONCLUSION

We have reported findings for the CO oxidation mechanisms on the MgO-supported AuCu clusters based on DFT simulations and microkinetic modeling. We place particular focus on the effect of the Au:Cu ratio which we have now mapped for three composition (1:3, 1:1, 3:1) for the particular cluster size of N=30. We have systematically considered the clusters on the defect-free, F-center (O-vacancy), and V-center (Mg-vacancy) MgO(100) supports. The support induces negative charge transfer to the Au_7Cu_{23} and $Au_{23}Cu_7$ clusters in all cases, and that the effect is pronounced for the F-center. The alloy composition turns out crucial in terms of the reactant adsorption energies and sites, selectivity (possible poisoning) and reaction barriers. These effects are amplified in the reaction kinetics and sensitivity to external parameters (microkinetic modeling) highlighting the possibility for catalyst design in terms of bimetallic alloy composition.

The adsorption of O_2 and CO have been calculated by tuning the location of vacancies in MgO(100). Here, the only systems binding O_2 more strongly than CO are Au_7Cu_{23}/MgO(100) and $Au_{23}Cu_7$/MgO(100) with the F-center. The interfacial binding of O_2 in the AuCu/MgO perimeter strengthens the substrate effect by inducing more charge transfer to O_2. Moreover, O_2 can be effectively activated upon adsorption and dissociated to 2×O atoms by crossing a low energy barrier, especially on the F-center support. The O_2 dissociation barrier decreases for Cu-rich alloys.

CO oxidation reaction paths have been explored based on the LH and ER mechanisms and the dissociated O atoms are also taken into account for the reaction paths. In general, the reaction barriers for CO oxidation are small for the clusters on F-centers, and the LH mechanism is lower in energy overall than ER due to the co-adsorption of CO and O_2 (or 2×O). The increased Cu-content causes over-binding of reactants which may turn out harmful for CO oxidation in more realistic conditions (*e.g.* oxidation). The microkinetic modeling built on the collected DFT results confirms that the CO_2 production rate is significant for the F-center Au_7Cu_{23}/MgO(100) and $Au_{23}Cu_7$/MgO(100) systems at low temperature (300 K). In comparison with the $Au_{15}Cu_{15}$/MgO(100) system,[27] the sequence of CO_2 production rate is $r(Au_{15}Cu_{15}) > r(Au_7Cu_{23}) > r(Au_{23}Cu_7)$. While the CO_2 production is the highest for $Au_{15}Cu_{15}$, it is also very sensitive to CO poisoning (strong CO binding). For Au_7Cu_{23} and $Au_{23}Cu_7$, the stronger binding of O_2 than CO modifies the catalyst sensitivity towards CO and O_2 partial pressures.

Altogether, we find that the catalyst composition (Au:Cu ratio), the catalyst structure (location of Au and Cu), the support and its structure (defects), and the interfacial effects on adsorption have deep influences on the catalytic performance of supported bimetallic AuCu nanoparticles. The catalytic process is a complex problem, which needs to be studied case-by-case by taking into account these factors.

AUTHOR INFORMATION

Corresponding Author

*E-mail: jaakko.akola@tut.fi. Phone: +358 40 198 1179.

ACKNOWLEDGEMENTS

The DFT calculations were carried out in CSC - the IT Center for Science Ltd., Espoo, Finland. Financial support has been provided by the Academy of Finland through its Centre of Excellence

Program (Project 284621) and the European Union Horizon 2020 NMP programme through the CritCat Project under Grant Agreement No. 686053.

Supporting Information

Properties of the most stable co-adsorption configurations (Table S1); Most stable O_2 and CO adsorption configurations (Figure S1); PDOS of the Au_7Cu_{23} and $Au_{23}Cu_7$ clusters on the F-center MgO(100) supports (Figure S2); CDD of the Au_7Cu_{23} and $Au_{23}Cu_7$ clusters adsorbed on F-center MgO(100) supports (Figure S3); Pathways of O_2 dissociation on Au_7Cu_{23}/MgO(100) with the defect-free and V-center surfaces, $Au_{23}Cu_7$/MgO(100) with the defect-free surface (Figure S4); CO oxidation on Au_7Cu_{23}/MgO(100) and $Au_{23}Cu_7$/MgO(100) with the F-center surfaces by ER mechanism (Figures S5-S6); PDOS of the O_2 adsorbed $Au_{15}Cu_{15}$ cluster on the F-center MgO(100) support (Figure S7).

REFERENCES

(1) Gong, J. Structure and Surface Chemistry of Gold-Based Model Catalysts. *Chem. Rev.* **2012**, *112*, 2987–3054.

(2) Bracey, C.L.; Ellis, P. R.; Hutchings, G. J. Application of Copper–Gold Alloys in Catalysis: Current Status and Future Perspectives. *Chem. Soc. Rev.* **2009**, *38*, 2231-2243.

(3) Ferrando, R.; Jellinek, J.; Johnson, R. L. Nanoalloys: From Theory to Applications of Alloy Clusters and Nanoparticles. *Chem. Rev.* **2008**, *108*, 849-910.

(4) Zhao, D.; Xu, B. Q. Enhancement of Pt Utilization in Electrocatalysts by Using Gold Nanoparticles. *Angew. Chem., Int. Ed.* **2006**, *45*, 4955−4959.

(5) Zhang, J.; Sasaki, K.; Sutter, E.; Adzic, R. R. Stabilization of Platinum Oxygen-Reduction Electrocatalysts Using Gold Clusters. *Science* **2007**, *315*, 220−222.

(6) Chen, J. G.; Menning, C. A.; Zellner, M. B. Monolayer Bimetallic Surfaces: Experimental and Theoretical Studies of Trends in Electronic and Chemical Properties. *Surf. Sci. Rep.* **2008**, *63*, 201−254.

(7) Hutchings, G. J.; Brust, M.; Schmidbaur, H. Gold - an Introductory Perspective. *Chem. Soc. Rev.* **2008**, *37*, 1759-1765.

(8) Haruta, M.; Kobayashi, T.; Sano, H.; Yamada N. Novel Gold Catalysts for the Oxidation of Carbon Monoxide at a Temperature Far Below 0 °C. *Chem. Lett.* **1987**, *2*, 405-408.

(9) Li, L.; Gao, Y.; Li, H.; Zhao, Y.; Pei, Y.; Chen, Z. F., Zeng, X. C. CO Oxidation on TiO2(110) Supported Subnanometer Gold Clusters: Size and Shape Effects. *J. Am. Chem. Soc.* **2013**, *135*, 19336-19346.

(10) Li, L.; Zeng, X. C. Direct Simulation Evidence of Generation of Oxygen Vacancies at the Golden Cage Au_{16} and TiO_2(110) Interface for CO oxidation. *J. Am. Chem. Soc.* **2014**, *136*, 15857–15860.

(11) Konova, P.; Naydenov, A.; Venkov, Cv.; Mehavdjiev, D; Andreeva, D.; Tabakova, T. Activity and Deactivation of Au/TiO_2 Catalyst in CO Oxidation. *J. Mol. Cat. A: Chem.* **2004**, *213*, 235-240.

(12) Starr, D. E.; Shaikhutdinov, S. K.; Freund, H. J. Gold Supported on Oxide Surfaces: Environmental Effects as Studied by STM. *Top. Cata.* **2005**, *36*, 33-41.

(13) Yoon, B.; Häkkinen, H.; Landman, U.; Wörz, A. S.; Antonietti, J. M.; Abbet, S.; Judai, K.; Heiz, U. Charging Effects on Bonding and Catalyzed Oxidation of CO on Au_8 Clusters on MgO. *Science* **2005**, *307*, 403-407.

(14) Stamatakis, M.; Christiansen, M A.; Vlachos, D G.; Mpourmpakis, G. Multiscale Modeling Reveals Poisoning Mechanisms of MgO-Supported Au Clusters in CO Oxidation. *Nano lett.* **2012**, *12*, 3621-3626.

(15) Liu, H.; Kozlov, A. I.; Kozlova, A. P.; Shido, T.; Asakura, K.; Iwasawa, Y. Active Oxygen Species and Mechanism for Low-Temperature CO Oxidation Reaction on a TiO_2-Supported Au Catalyst Prepared from $Au(PPh_3)(NO_3)$ and As-Precipitated Titanium Hydroxide. *J. Cata.* **1999**, *185*, 252-264.

(16) Kim, T. S.; Stiehl, J. D.; Reeves, C. T.; Meyer, R. J.; Mullins, C. B. Cryogenic CO Oxidation on TiO_2-Supported Gold Nanoclusters Precovered with Atomic Oxygen. *J. Am. Chem. Soc.* **2003**, *125*, 2018–2019.

(17) Liu, Z. P.; Hu, P.; Alavi, A. Catalytic Role of Gold in Gold-Based Catalysts: A Density Functional Theory Study on the CO Oxidation on Gold. *J. Am. Chem. Soc.* **2002**, *124*, 14770–14779.

(18) Li, X.; Fang, S. S. S.; Teo, J.; Foo, Y. L.; Borgna, A.; Lin, M.; Zhong, Z. Y. Activation and Deactivation of Au–Cu/SBA-15 Catalyst for Preferential Oxidation of CO in H_2-Rich Gas. *ACS Catal.* **2012**, *2*, 360–369.

(19) Liu, X.; Wang, A.; Wang, X.; Mou, C.; Zhang, T. Au–Cu Alloy Nanoparticles Confined in SBA-15 as a Highly Efficient Catalyst for CO Oxidation. *Chem. Commun.* **2008**, 3187-3189.

(20) Sandoval, A.; Louis, C.; Zanella, R. Improved Activity and Stability in CO oxidation of Bimetallic Au-Cu/TiO_2 Catalysts Prepared by Deposition-Precipitation with Urea. *Appl. Cata. B* **2013**, *140-141*, 363-377.

(21) Mozer, T. S.; Dziuba, D. A.; Vieira, C. T. P.; Passos, F. B. J. The Effect of Copper on the Selective Carbon Monoxide Oxidation over Alumina Supported Gold Catalysts. *J. Power Sources* **2009**, *187*, 209−215.

(22) Liu, X.; Wang, A.; Li, L.; Zhang, T.; Mou, C. Y.; Lee, J. F. Structural Changes of Au-Cu Bimetallic Catalysts in CO Oxidation: In Situ XRD, EPR, XANES, and FT-IR Characterizations. *J. Catal.* **2011**, *278*, 288−296.

(23) Najafishirtari, S.; Brescia, R.; Guardia, P.; Marras, S.; Manna, L.; Colombo, M. Nanoscale Transformations of Alumina-Supported AuCu Ordered Phase Nanocrystals and Their Activity in CO Oxidation. *ACS Catal.* **2015**, *5*, 2154-2163.

(24) Yin, J.; Shan, S.; Yang, L.; Mott, D.; Malis, O.; Petkov, V.; Cai, F.; Shan, N. M.; Luo, J.; Chen, B. H.; et al. Gold–Copper Nanoparticles: Nanostructural Evolution and Bifunctional Catalytic Sites. *Chem. Mater.* **2012**, *24*, 4662−4674.

(25) Bracey, C. L.; Ellis, P. R.; Hutchings, G. J. Application of Copper-Gold Alloys in Catalysis: Current Status and Future Perspectives. *Chem. Soc. Rev.* **2009**, *38*, 2231-2243.

(26) Pauwels, B.; Van Tendeloo, G.; Zhurkin, E.; Hou, M.; Verschoren, G.; Theil Kuhn, L.; Bouwen, W.; Lievens, P. Transmission Electron Microscopy and Monte Carlo Simulations of Ordering in Au-Cu Clusters Produced in a Laser Vaporization Source. *Phys. Rev. B* **2001**, *63*, 165406.

(27) Ma, L.; Melander, M.; Weckman, T.; Laasonen, K.; Akola, J. CO Oxidation on the $Au_{15}Cu_{15}$ Cluster and the Role of Vacancies in the MgO(100) Support. *J. Phys. Chem. C* **2016**, *120*, 26747-26758.

(28) Cerbelaud, M.; Barcaro, G.; Fortunelli, A.; Ferrando R. Theoretical Study of AuCu Nanoalloys Adsorbed on MgO (001). *Surf. Sci.* **2012**, *606*, 938-944.

(29) Henry, C. R. Surface Studies of Supported Model Catalysts. *Surf. Sci. Rep.* **1998**, 31, 231-325.

(30) Barth, C.; Henry, C. R. Atomic Resolution Imaging of the (001) Surface of UHV Cleaved MgO by Dynamic Scanning Force Microscopy. *Phys. Rev. Lett.* **2003**, *91*, 196012.

(31) Chiesa, M.; Paganini, M. C.; Giamello, E.; Valentin, C. D.; Pacchioni, G. First Evidence of a Single-Ion Electron Trap at the Surface of an Ionic Oxide. *Angew. Chem., Int. Ed.* **2003**, *42*, 1759-1761.

(32) Kramer, J.; Ernst, W.; Tegenkamp, C.; Pfnür, H. Mechanism and Kinetics of Color Center Formation on Epitaxial Thin Films of MgO. *Surf. Sci.* **2002**, *517*, 87-97.

(33) Sterrer, M.; Fischbach, E.; Risse, T.; Freund, H. J. Geometric Characterization of a Singly Charged Oxygen Vacancy on a Single-Crystalline MgO(001) Film by Electron Paramagnetic Resonance Spectroscopy. *Phys. Rev. Lett.* **2005**, *94*, 186101.

(34) Haas, G.; Menck, A.; Brune, H.; Barth, J. V.; Venables, J. A.; Kern, K. Nucleation and Growth of Supported Clusters at Defect Sites: Pd/MgO(001). *Phys. Rev. B* **2000**, *61*, 11105-11108.

(35) Venables, J. A.; Giordano, L.; Harding, J. H. Nucleation and Growth on Defect Sites: Experiment–Theory Comparison for Pd/MgO(001). *J. Phys.: Condens. Matter* **2006**, *18*, S411-S427.

(36) Lopez, N.; Illas, F.; Rösch, N.; Pacchioni, G. Adhesion Energy of Cu Atoms on the MgO(100) Surface. *J. Chem. Phys.* **1999**, *110*, 4873-4879.

(37) Markovits, A.; Skalli, M. K.; Minot, C.; Pacchioni, G.; López, N.; Illas, F. The Competition Between Chemical Bonding and Magnetism in the Adsorption of Atomic Ni on MgO(100). *J. Chem. Phys.* **2001**, *115*, 8172-4877.

(38) Giordano L.; Goniakowski, J.; Pacchioni, G. Characteristics of Pd Adsorption on the MgO(100) Surface: Role of Oxygen Vacancies. *Phys. Rev. B* **2001**, *64*, 075417.

(39) Bogicevic, A.; Jennison, D. R. Effect of Oxide Vacancies on Metal Island Nucleation. *Surf. Sci.* **2002**, *515*, L481-L486.

(40) Dong, Y. F.; Wang, S. J.; Mi, Y. Y.; Feng, Y. P.; Huan, A. C. H. First-Principles Studies on Initial Growth of Ni on MgO(001) Surface. *Surf. Sci.* **2006**, *600*, 2154-2162.

(41) Renaud, G.; Lazzari, R.; Revenant, C.; Barbier, A.; Noblet, M.; Ulrich, O.; Leroy, F.; Jupille, J.; Borensztein, Y.; Henry, C. R.; et al. Real-Time Monitoring of Growing Nanoparticles. *Science* **2003**, *300*, 1416-1419.

(42) Barcaro, G.; Fortunelli, A. Structure and Diffusion of Small Ag and Au Clusters on the Regular MgO (100) Surface. *New J. Phys.* **2007**, *9*, 22.

(43) VandeVondele, J.; Krack, M.; Mohamed, F.; Parrinello, M.; Chassaing, T; Hutter, J. Fast and Accurate Density Functional Calculations Using a Mixed Gaussian and Plane Waves Approach. *Comput. Phys. Commun.* **2005**, *167*, 103-128.

(44) CP2K: Open Source Molecular Dynamics (http://www.cp2k.org), accessed May 01, 2016.

(45) Perdew, J. P.; Burke, K.; Ernzerhof, M. Generalized Gradient Approximation Made Simple. *Phys. Rev. Lett.* **1996**, *77*, 3865.

(46) VandeVondele, J.; Hutter, J. Gaussian Basis Sets for Accurate Calculations on Molecular Systems in Gas and Condensed Phases. *J. Chem. Phys.* **2007**, *127*, 114105.

(47) Goedecker, S.; Teter, M.; Hutter, J. Separable Dual-Space Gaussian Pseudopotentials. *Phys. Rev. B* **1996**, *54*, 1703.

(48) Xu, L.; Henkelman, G. Calculations of Ca Adsorption on a MgO(100) Surface: Determination of the Binding Sites and Growth Mode. *Phys. Rev. B* **2008**, *77*, 205404.

(49) Yu, M.; Trinkle, D. R. Accurate and Efficient Algorithm for Bader Charge Integration. *J. Chem. Phys.* **2011**, *134*, 064111.

(50) Henkelman, G.; Uberuaga, B. P.; Jónsson, H. A. Climbing Image Nudged Elastic Band Method for Finding Saddle Points and Minimum Energy Paths. *J. Chem Phys.* **2000**, *113*, 9901-9904.

(51) Ma, L.; Melander, M.; Laasonen, K.; Akola, J. CO Oxidation Catalyzed by Neutral and Anionic Cu_{20} Clusters: Relationship between Charge and Activity. *Phys. Chem. Chem. Phys.* **2015**, *17*, 7067-7076.

(52) Lide, D. R., *CRC Handbook of Chemistry and Physics, 84th Edition*; CRC Press: Florida, 2003.

(53) Li. H.; Li, L.; Pederson, A.; Gao, Y.; Khetrapal, N.; Jónsson, H.; Zeng, X. C. Magic-Number Gold Nanoclusters with Diameters from 1 to 3.5 nm: Relative stability and Catalytic Activity for CO oxidation. *Nano Lett.* **2015**, *15*, 682-688.

(54) Kim, H. Y.; Lee, H. M.; Henkelman, G. CO Oxidation Mechanism on CeO_2-Supported Au Nanoparticles. *J. Am. Chem. Soc.* **2012**, *134*, 1560−1570.

(55) Zhang, L.; Kim, H. Y.; Henkelman, G. CO Oxidation at the Au−Cu Interface of Bimetallic Nanoclusters Supported on CeO_2(111). *J. Phys. Chem. Lett.* **2013**, *4*, 2943-2947.

(56) Gao, Y.; Shao, N.; Pei, Y.; Chen, Z.; Zeng, X. Catalytic Activities of Subnanometer Gold Clusters (Au_{16}-Au_{18}, Au_{20}, and Au_{27}-Au_{35}) for CO oxidation. *ACS nano*. **2011**, *5*, 7818-7829.

(57) Nikbin, N.; Mpourmpakis, G.; Vlachos, D. G. A Combined DFT and Statistical Mechanics Study for the CO Oxidation on the Au_{10}^{-1} Cluster. *J. Phys. Chem. C* **2011**, *115*, 20192-20200.

(58) Hirabayashi, S.; Ichihashi, M.; Kawazoe, Y.; Kondow, T. Comparison of Adsorption Probabilities of O_2 and CO on Copper Cluster Cations and Anions. *J. Phys. Chem. A* **2012**, *116*, 8799-8806.

(59) Wang Y.; Wu, G.; Yang, M.; Wang, J. Competition between Eley−Rideal and Langmuir−Hinshelwood Pathways of CO Oxidation on Cu_n and Cu_nO (n = 6, 7) Clusters. *J. Phys. Chem. C* **2013**, *117*, 8767−8773.

(60) Ma, L.; Melander, M.; Weckman, T.; Lipasti, S.; Laasonen, K.; Akola, J. DFT Simulations and Microkinetic Modelling of 1-Pentyne Hydrogenation on Cu_{20} Model Catalysts. *J. Mol. Graph. Model.* **2016**, *65*, 61-70.

Table 1 Adsorption energy (E_{ad}^{1}), net charge (Q), bond length of Cu-O (r_{Cu-O}) and Au-O (r_{Au-O}), average bond length <R>, and symmetry of the Au_7C_{23}, $Au_{15}Cu_{15}$ and $Au_{23}Cu_7$ clusters on three MgO(100) supports.

	Defect-free	F-center	V-center
	Au_7Cu_{23} / $Au_{15}Cu_{15}$ / $Au_{23}Cu_7$	Au_7Cu_{23} / $Au_{15}Cu_{15}$ / $Au_{23}Cu_7$	Au_7Cu_{23} / $Au_{15}Cu_{15}$ / $Au_{23}Cu_7$
E_{ad}^{1} (eV)	4.95 / 5.42 / 4.71	6.35 / 7.65 / 7.06	9.55 / 9.05 / 7.78
Q (e)	-1.96 / -1.96 / -2.15	-3.41 / -3.54 / -3.66	-0.84 / -0.87 / -1.32
r_{Cu-O} (Å)	2.11-2.43 / 2.07-2.09 / 2.21	2.18-2.79 / 2.16-2.25 / 2.22-2.75	2.00-2.18 / 1.91-1.94 / 2.01
r_{Au-O} (Å)	2.79-2.93 / 2.66-3.10 / 2.59-2.76	2.84-3.16 / 2.68-3.12 / 2.67-2.88	2.75-2.91 / 2.57-2.92 / 2.31-2.67
$< R >$ (Å)	2.58 / 2.66 / 2.79	2.59 / 2.65 / 2.78	2.60 / 2.66 / 2.79
symmetry	C_{2v} / C_{2v} / C_{2v}	C_s / C_s / C_s	C_{2v} / C_{2v} / C_{2v}

Table 2 Adsorption energy (E_{ad}^{2}) of O_2, 2×O and CO, bond length of O_2 (r_{O-O}) and CO ($r_{C=O}$) molecules, charge transfer (Q) from the adsorbent [Au_7Cu_{23}/MgO(100) or $Au_{23}Cu_7$/MgO(100)] to the adsorbate (O_2, 2×O or CO), and activation energy barrier ($O_2 \rightarrow O + O$) for the lowest energy adsorption systems. O_2 cannot adsorb on the $Au_{23}Cu_7$/MgO(100) system with V-center (missing).

Au_7Cu_{23}/MgO(100)	E_{ad}^{2} (eV)			r_{O-O} (Å)	$r_{C=O}$ (Å)	Q (e)			Reaction (eV)
	O_2	2×O	CO	O_2	CO	O_2	2×O	CO	$O_2 \rightarrow O + O$
Defect-free	1.28	3.79	1.23	1.46	1.19	1.20	2.18	0.43	0.10, 0.43
F-center	1.89	4.22	1.27	1.51	1.19	1.46	2.22	0.36	0.13
V-center	1.00	2.54	1.17	1.44	1.19	1.11	2.16	0.35	0.32
$Au_{23}Cu_7$/MgO(100)									
Defect-free	0.16	1.17	0.90	1.40	1.15	0.89	1.84	0.08	0.69
F-center	0.68	1.12	0.56	1.47	1.15	1.18	1.89	0.08	0.62

Table 3 Calculated activation energy barriers (E_f) and the reaction energies (ΔH) for CO oxidation on the F-center Au_7Cu_{23}/MgO(100) and $Au_{23}Cu_7$/MgO(100). The symbol '*' refers to the atom or molecule being adsorbed on the cluster.

Reaction	Au_7Cu_{23}/MgO(100)		$Au_{23}Cu_7$/MgO(100)	
	E_f (eV)	ΔH (eV)	E_f (eV)	ΔH (eV)
CO* + O_2* ↔ CO_2 + O*	0.21	-2.66	0.27	-2.36
CO* + O* ↔ CO_2	0.52	-0.11	0.77	-2.03
CO* + O* + O* ↔ CO_2 + O*	0.35	-0.28	0.53	-1.69
CO + O_2* ↔ CO_2 + O*	0.14	-3.89	0.30	-3.39
CO + O* ↔ CO_2	0.29	-1.38	0.42	-3.17
CO + O* + O* ↔ CO_2 + O*	0.31	-1.49	0.29	-2.76

Table 4 The calculated coverage of species (θ_{CO}, θ_{O_2}, θ_O) and the rate (s^{-1}) of CO_2 formation (r_{CO_2}) at long time scales with different temperatures (150 K and 300 K) and different O_2 partial pressures under *P(CO)* = 0.01 bar.

	Au_7Cu_{23}/MgO(100)		$Au_{23}Cu_7$/MgO(100)	
P(O₂)=0.01 bar	150 K	300 K	150 K	300 K
θ_{CO}	1.0	3.67×10^{-1}	1.26×10^{-1}	2.21×10^{-1}
θ_{O_2}	5.71×10^{-22}	5.54×10^{-4}	5.56×10^{-7}	1.04×10^{-4}
θ_O	1.15×10^{-16}	6.32×10^{-1}	8.73×10^{-1}	7.79×10^{-1}
r_{CO_2}	1.14×10^{-15}	1.05×10^{6}	3.90×10^{-4}	1.00×10^{4}
P(O₂)=0.05 bar				
θ_{CO}	5.64×10^{-1}	3.74×10^{-2}	2.45×10^{-4}	7.81×10^{-4}
θ_{O_2}	3.15×10^{-6}	2.30×10^{-3}	7.38×10^{-5}	7.56×10^{-3}
θ_O	4.35×10^{-1}	9.58×10^{-1}	9.99×10^{-1}	9.84×10^{-1}
r_{CO_2}	4.83	1.59×10^{6}	4.72×10^{-4}	1.06×10^{4}
P(O₂)=0.1 bar				
θ_{CO}	2.50×10^{-1}	1.66×10^{-2}	1.08×10^{-4}	3.47×10^{-4}
θ_{O_2}	6.10×10^{-6}	2.64×10^{-3}	8.30×10^{-5}	8.49×10^{-3}
θ_O	7.49×10^{-1}	9.78×10^{-1}	9.99×10^{-1}	9.82×10^{-1}
r_{CO_2}	8.31	1.62×10^{6}	4.72×10^{-4}	1.06×10^{4}
P(O₂)=0.5 bar				
θ_{CO}	4.46×10^{-2}	3.05×10^{-3}	2.00×10^{-5}	6.38×10^{-5}
θ_{O_2}	8.45×10^{-6}	2.92×10^{-3}	9.04×10^{-5}	9.24×10^{-3}
θ_O	9.53×10^{-1}	9.91×10^{-1}	9.99×10^{-1}	9.81×10^{-1}
r_{CO_2}	1.05×10^{1}	1.65×10^{6}	4.72×10^{-4}	1.06×10^{4}

Figure 1 (Top row) Optimized geometries of Au_7Cu_{23}/MgO(100) and $Au_{23}Cu_7$/MgO(100) and the corresponding MgO(100) surface (a dashed square denoting the cluster position) with the defect-free, F-center, and V-center support. (Bottom row) Top view and angular view with one layer of support of the defect-free Au_7Cu_{23}/MgO(100) and $Au_{23}Cu_7$/MgO(100) geometries. Color key: yellow, Au; coral, Cu; green, Mg; and red, O.

Figure 2 Projected electronic density of states (PDOS) of the O_2 adsorbed onto (a) Au_7Cu_{23} and (b) $Au_{23}Cu_7$ cluster on the F-center MgO(100) support and zoom-ins near the Fermi energy for cluster atoms (insets). HOMO-1, HOMO, and LUMO levels of the gas phase triplet O_2 molecule are included for reference in blue color. The PDOS are projected onto the O_2 molecule and Au/Cu atoms of the Au_7Cu_{23} and $Au_{23}Cu_7$ clusters. The Fermi energy is set at zero.

Figure 3 Side and top views of the charge density difference (CDD) of the adsorbed O_2 molecule and HOMO/LUMO orbitals of the Au_7Cu_{23} and $Au_{23}Cu_7$ clusters on MgO(100) with the F-center. The adsorbed O_2 molecule is denoted in grey color. Blue and pink colors in CDD represent charge depletion and accumulation, respectively. The isosurface values are ± 0.002 e/a_0^3 for CDD and ± 0.02 e/a_0^3 for HOMO and LUMO.

Figure 4 Structures of the initial state (IS), transition state (TS), and final state (FS) of the lowest identified pathways for $O_2 \rightarrow O + O$ on Au_7Cu_{23}/MgO(100) and $Au_{23}Cu_7$/MgO(100) with the F-center and the energy changes with respect to the IS. The symbol '*' refers to the atom or molecule being adsorbed on the cluster.

Figure 5 Structures of the initial state (IS), transition state (TS), intermediate state (IM) and final state (FS) for the catalytic CO oxidation on Au_7Cu_{23}/MgO(100) with the F-center by Langmuir–Hinshelwood (LH) mechanism and the energy changes with respect to the IS. The symbol '*' refers to the atom or molecule being adsorbed on the cluster.

Figure 6 Structures of the initial state (IS), transition state (TS), and final state (FS) for the catalytic CO oxidation on $Au_{23}Cu_7$/MgO(100) with the F-center by Langmuir–Hinshelwood (LH) mechanism and the energy changes with respect to the IS. The symbol '*' refers to the atom or molecule being adsorbed on the cluster.

Figure 7 Potential energy diagrams of CO oxidation for the (a) Au_7Cu_{23}/MgO(100), (b) $Au_{15}Cu_{15}$/MgO(100), and (c) $Au_{23}Cu_7$/MgO(100) systems (with F-centers) by LH and ER mechanisms. The corresponding reaction pathways for O_2 (pre-) dissociation are inserted in each panel.

Figure 8 Coverages of the reactant species (O_2, CO, O) and TOF of CO_2 from microkinetic model simulations on (a) Au_7Cu_{23}/MgO(100) and (b) $Au_{23}Cu_7$/MgO(100) with the F-center as a function of time [$P(CO)$ = 0.01 bar, $P(O_2)$ = 0.01 bar, T = 300 K].

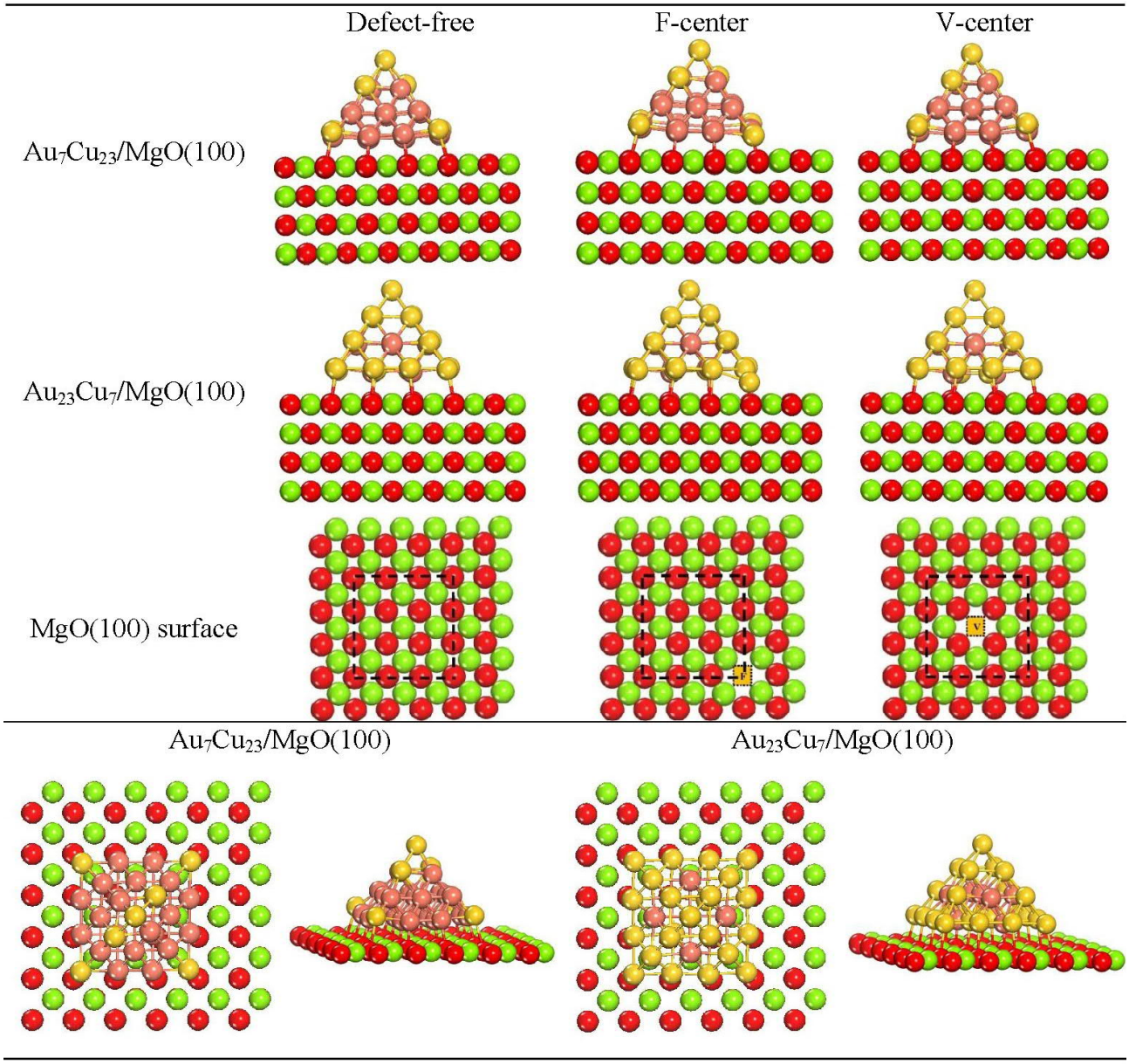
Defect-free
F-center
V-center
Au7Cu23/MgO(100)
Au23Cu7/MgO(100)
MgO(100) surface
F
V
Au7Cu23/MgO(100)
Au23Cu7/MgO(100)

Figure 1

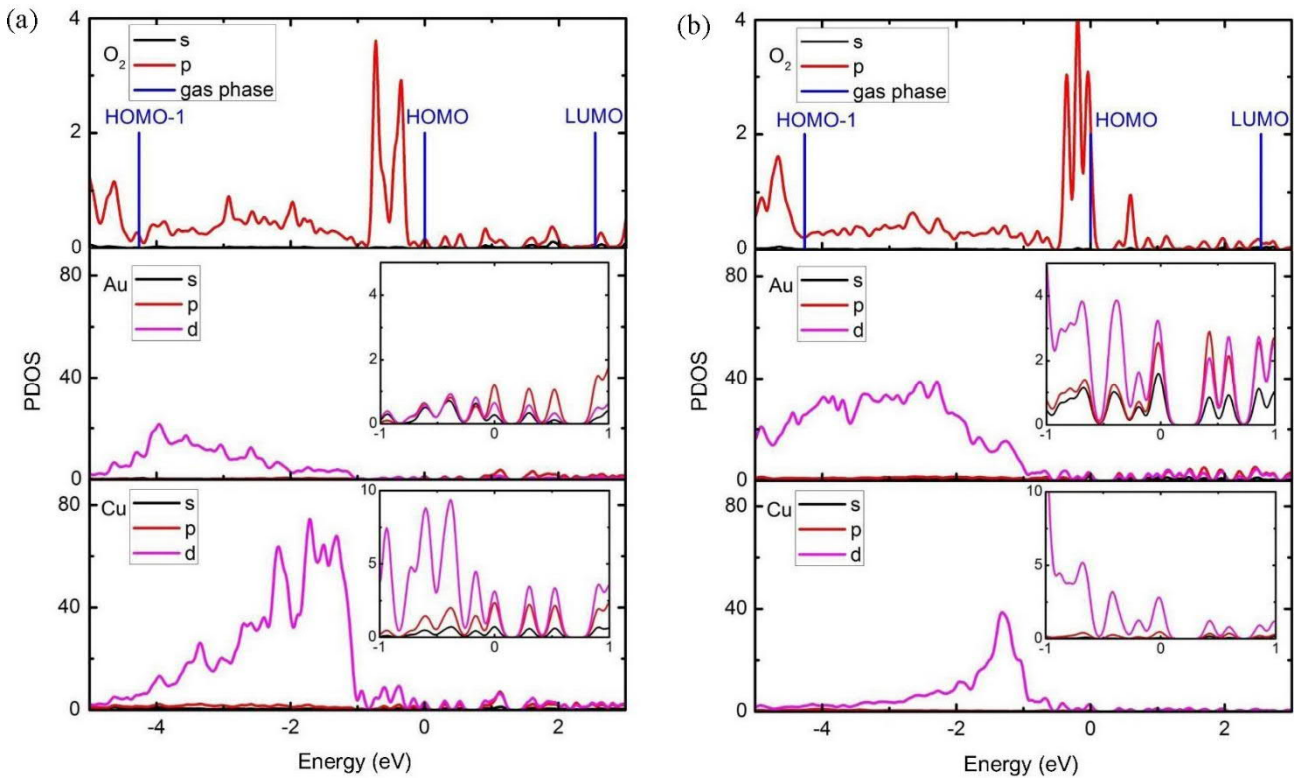

Figure 2

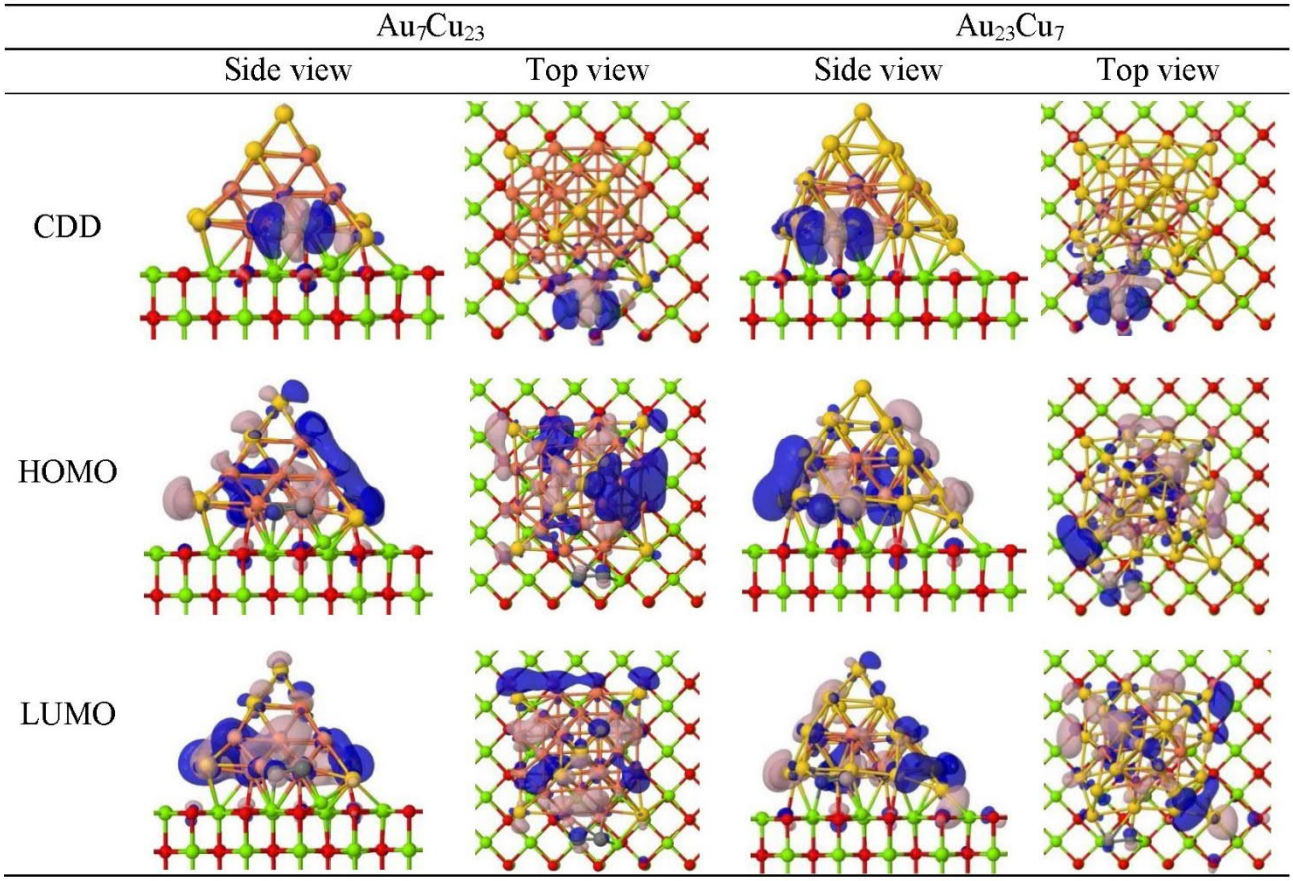
Au7Cu23
Au23Cu7
Side view
Top view
Side view
Top view
CDD
HOMO
LUMO

Figure 3

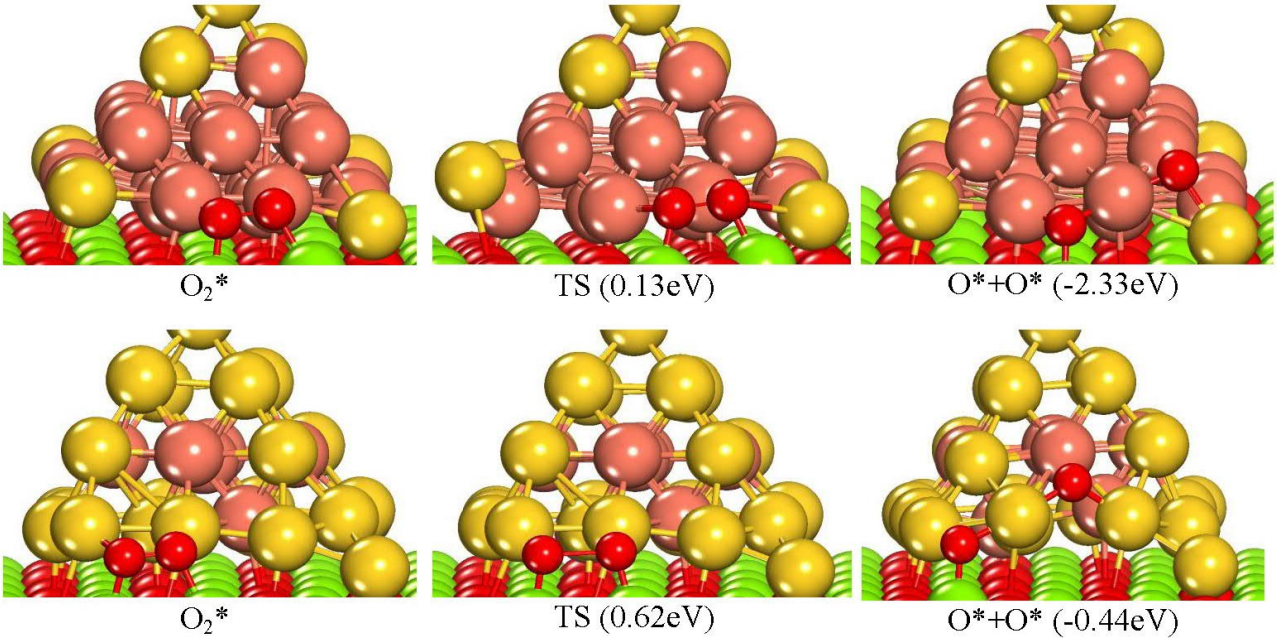

Figure 4

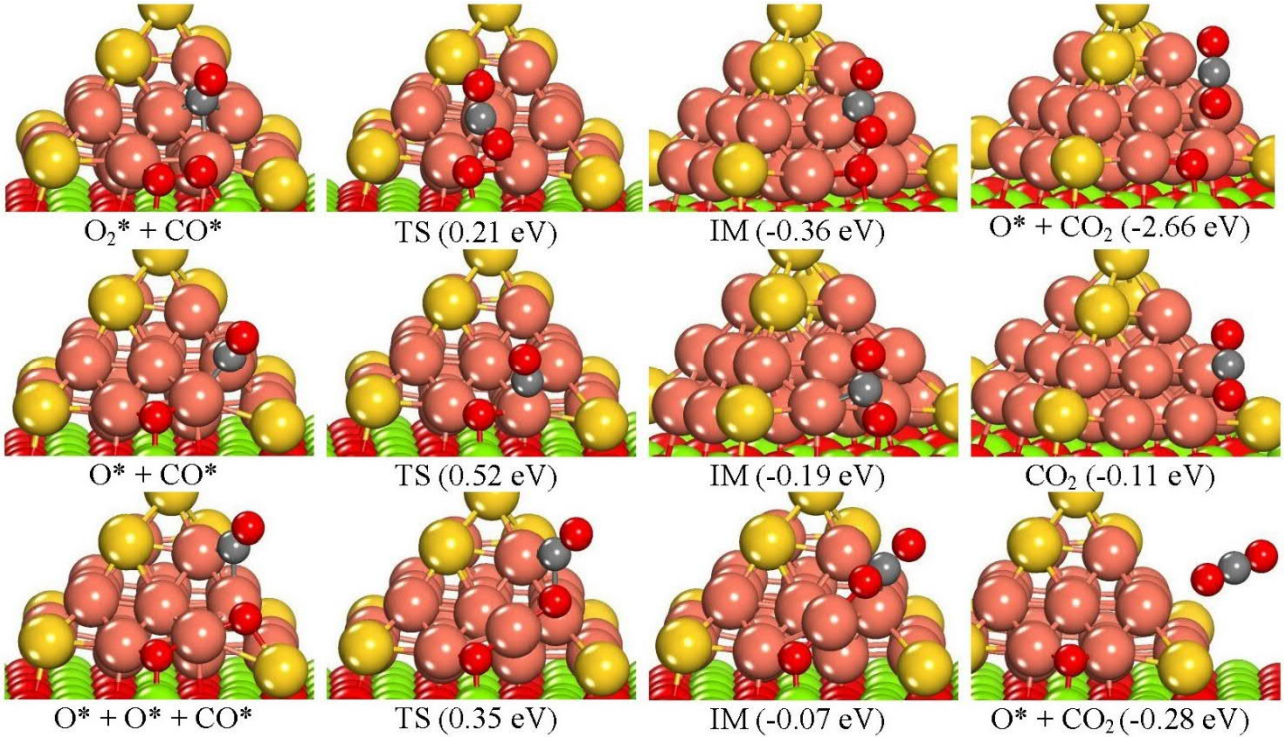
O_2* + CO*
TS (0.21 eV)
IM (-0.36 eV)
O* + CO_2 (-2.66 eV)
O* + CO*
TS (0.52 eV)
IM (-0.19 eV)
CO_2 (-0.11 eV)
O* + O* + CO*
TS (0.35 eV)
IM (-0.07 eV)
O* + CO_2 (-0.28 eV)

Figure 5

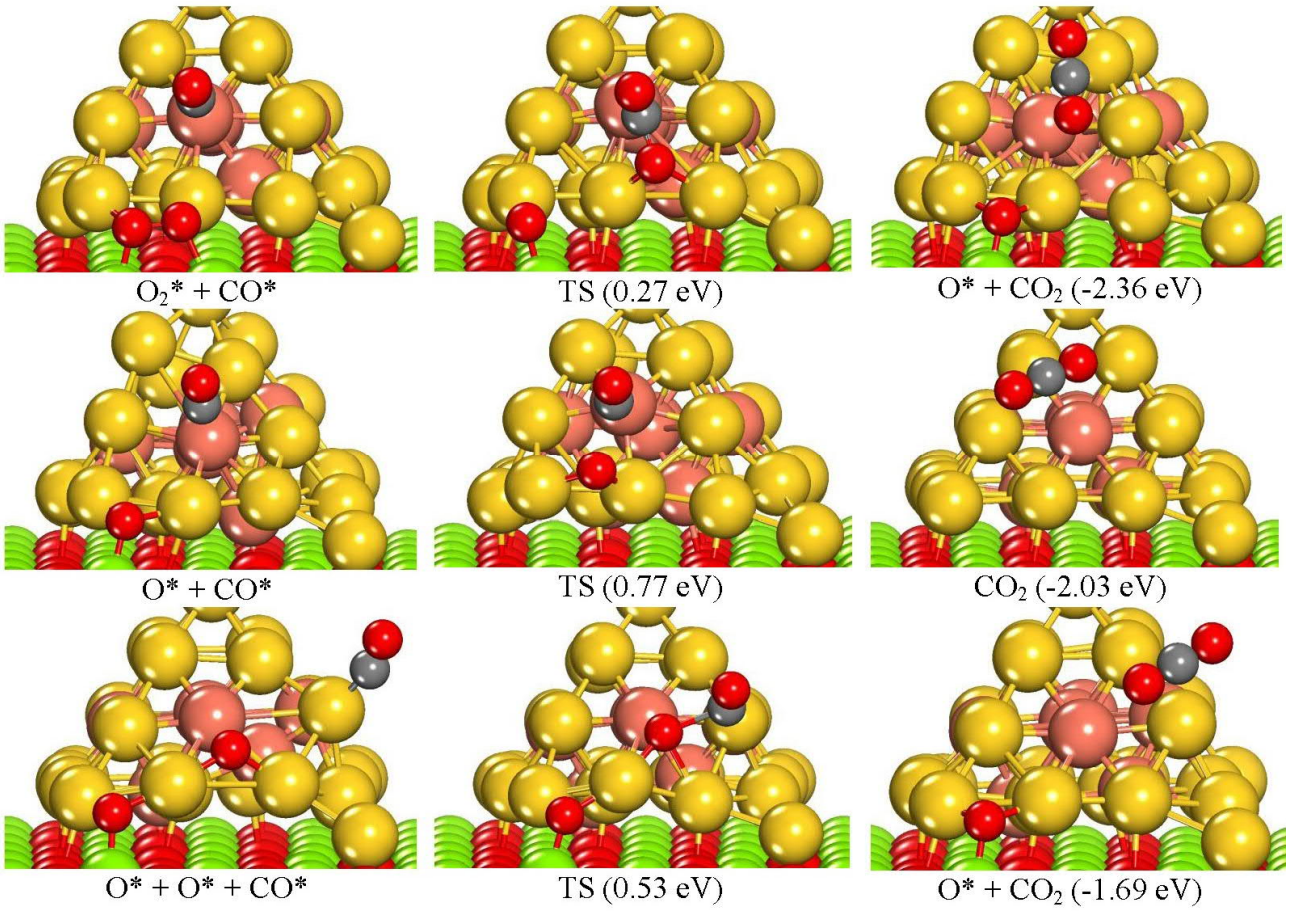
O_2* + CO*
TS (0.27 eV)
O* + CO_2 (-2.36 eV)
O* + CO*
TS (0.77 eV)
CO_2 (-2.03 eV)
O* + O* + CO*
TS (0.53 eV)
O* + CO_2 (-1.69 eV)

Figure 6

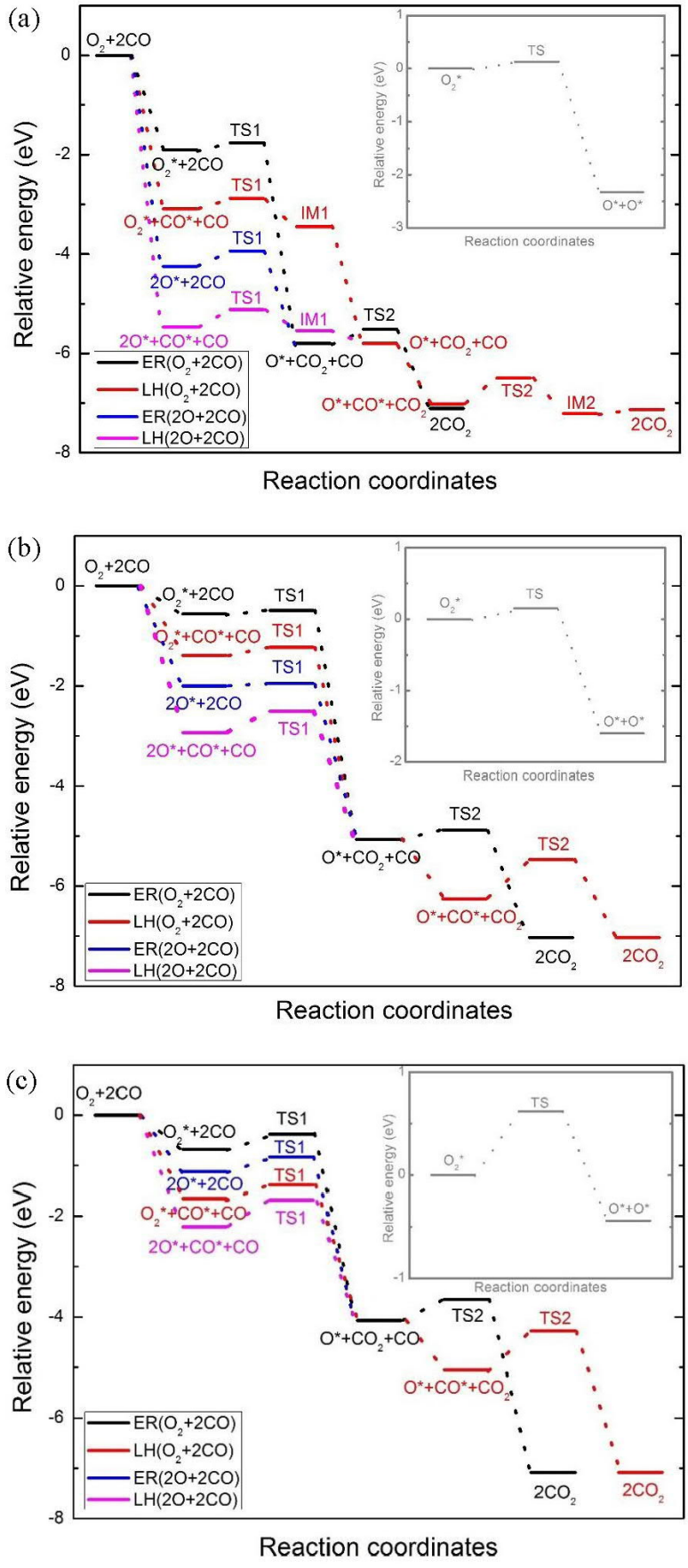
(a)
(b)
(c)
Relative energy (eV)
Reaction coordinates
O2+2CO
O2*+2CO
O2*+CO*+CO
2O*+2CO
2O*+CO*+CO
TS1
IM1
TS2
IM2
O*+CO2+CO
O*+CO*+CO2
2CO2
ER(O2+2CO)
LH(O2+2CO)
ER(2O+2CO)
LH(2O+2CO)
TS
O*+O*

Figure 7

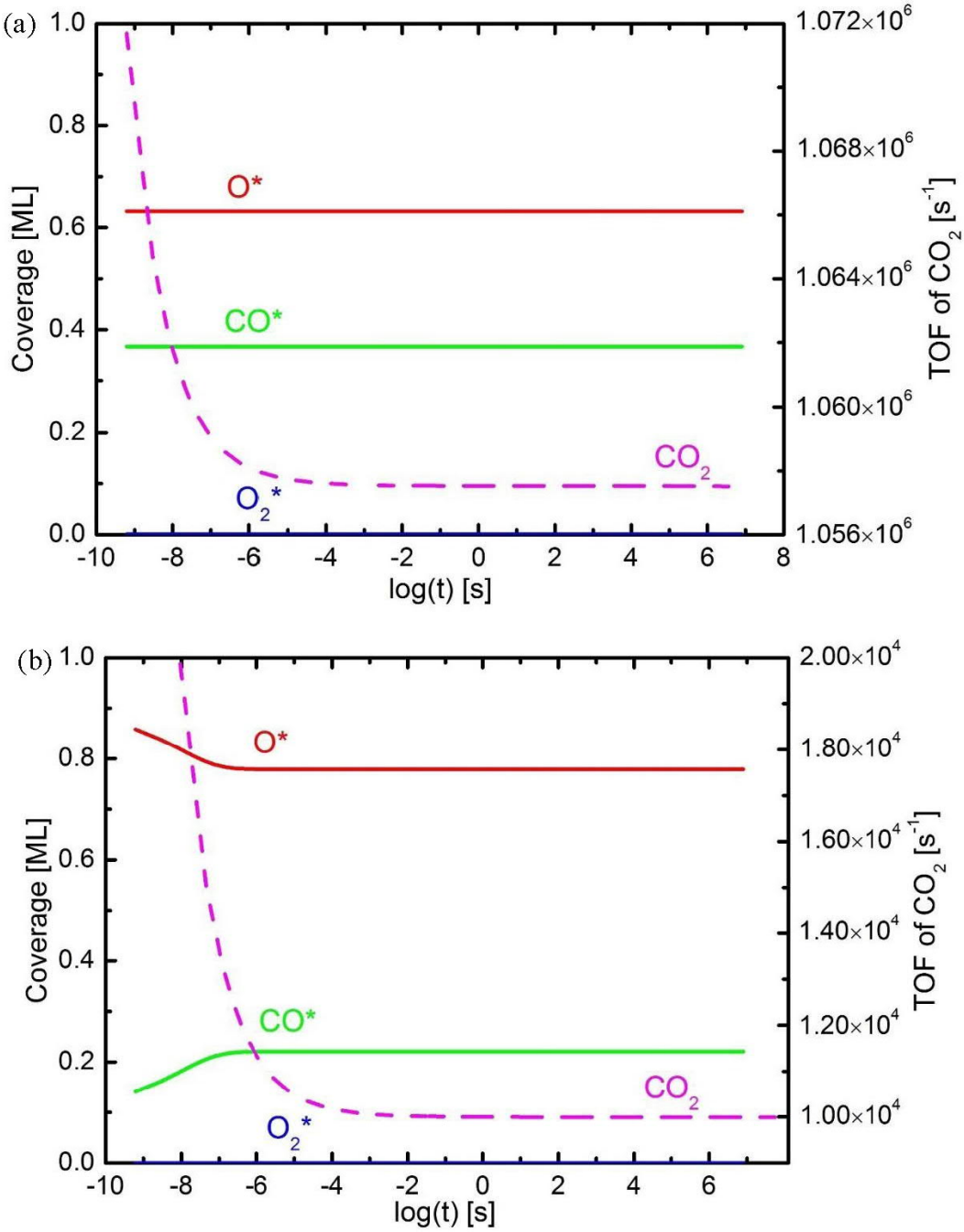
(a)
Coverage [ML]
TOF of CO_2 [s^{-1}]
log(t) [s]
O*
CO*
CO_2
O_2*
1.0
0.8
0.6
0.4
0.2
0.0
1.072×10^6
1.068×10^6
1.064×10^6
1.060×10^6
1.056×10^6
-10
-8
-6
-4
-2
0
2
4
6
8
(b)
Coverage [ML]
TOF of CO_2 [s^{-1}]
log(t) [s]
O*
CO*
CO_2
O_2*
1.0
0.8
0.6
0.4
0.2
0.0
2.00×10^4
1.80×10^4
1.60×10^4
1.40×10^4
1.20×10^4
1.00×10^4
-10
-8
-6
-4
-2
0
2
4
6

Figure 8

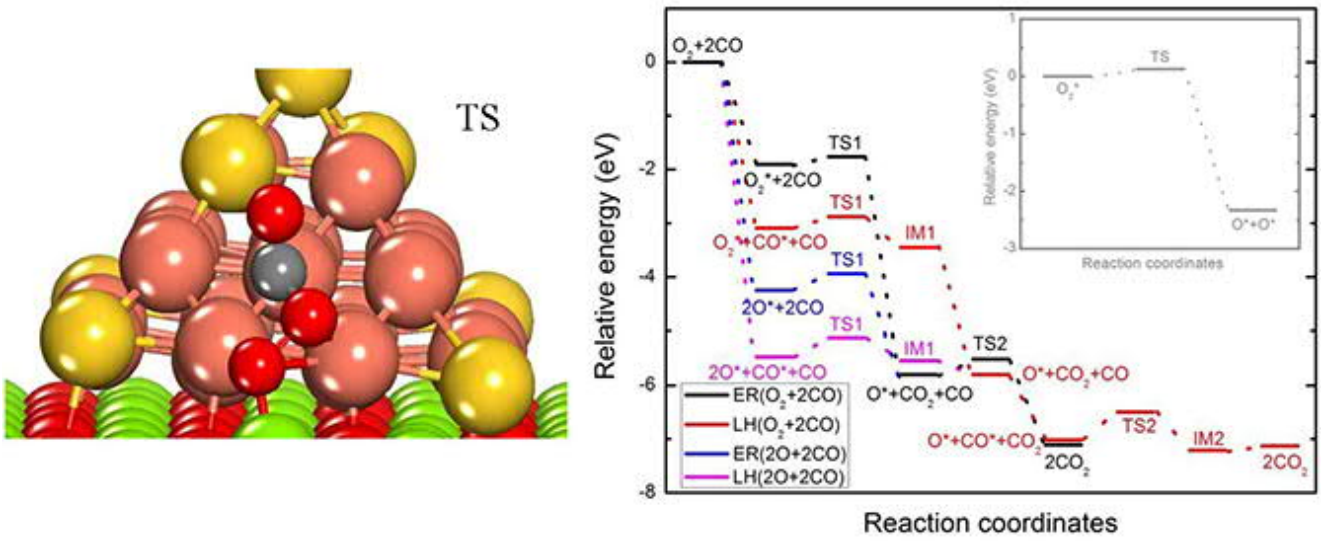

Table of Contents (TOC) Image

Supporting Information

Catalytic Activity of AuCu Clusters on MgO(100): Effect of Alloy Composition for CO Oxidation

Li Ma,[†,‡] Kari Laasonen,[§] and Jaakko Akola*[,†,‡,¶]

[†]Department of Physics, Tampere University of Technology, FI-33101 Tampere, Finland

[‡]COMP Centre of Excellence, Department of Applied Physics, Aalto University, FI-00076 Aalto, Finland

[§]COMP Centre of Excellence, Department of Chemistry, Aalto University, FI-00076 Aalto, Finland

[¶]Department of Physics, Norwegian University of Science and Technology, NO-7491, Trondheim, Norway

Corresponding Author

*E-mail: jaakko.akola@tut.fi. Phone: +358 40 198 1179.

In the Supporting Information, properties of the adsorption systems in the main text of Figures 5 and 6 are listed in Table S1. The most stable O_2 and CO adsorption configurations are shown in Figure S1. The projected density of states (PDOS) of the Au_7Cu_{23} and $Au_{23}Cu_7$ clusters on the F-center MgO(100) supports are given in Figure S2. The charge density differences (CDD) of the Au_7Cu_{23} and $Au_{23}Cu_7$ clusters adsorbed on F-center MgO(100) supports are plotted in Figure S3. Pathways of O_2 dissociation on Au_7Cu_{23}/MgO(100) with the defect-free and V-center surfaces, $Au_{23}Cu_7$/MgO(100) with the defect-free surface are shown in Figure S4. Reactions of CO oxidation on Au_7Cu_{23}/MgO(100) and $Au_{23}Cu_7$/MgO(100) with the F-center surfaces by ER mechanism are displayed in Figures S5 and S6. The PDOS of the O_2 adsorbed $Au_{15}Cu_{15}$ cluster on the F-center MgO(100) support is given in Figure S7.

A detailed analysis of the molecular orbitals has been performed to understand the electronic structure of AuCu clusters on different supports. As the PDOS shown in Figure S2, for the highest occupied energy levels, the contributions of *d*-orbital of Au and Cu atoms (cluster) are the most prominent, while the *p*-orbitals of O atoms (support) have also a visible weight. Moreover, to visualize the interaction between AuCu cluster and MgO support, Figure S3 gives the CDD of Au_7Cu_{23}/MgO and $Au_{23}Cu_7$/MgO with the F-center. CDD shows the interaction at the interface is especially pronounced (strong) for the vacancy regions of the F-centers. Combined with the information in PDOS and CDD, we conclude that the bonding between the MgO support and AuCu cluster is governed by the hybridization of Au-5*d*, Cu-3*d*, and O-2*p* orbitals, in agreement what has been reported for an MgO supported Au cluster.[1]

REFERENCE

(1) Yoon, B.; Häkkinen, H.; Landman, U.; Wörz, A. S.; Antonietti, J. M.; Abbet, S.; Judai, K.; Heiz, U. Charging Effects on Bonding and Catalyzed Oxidation of CO on Au_8 Clusters on MgO. *Science* **2005**, *307*, 403-407.

Table S1 Adsorption energy of different adsorbates, bond length of the adsorbed O_2 and CO molecules (r_{O-O} , $r_{C=O}$), charge transfer (*Q*) from the adsorbent [Au_7Cu_{23}/MgO(100) or $Au_{23}Cu_7$/MgO(100)] to the adsorbate (O or CO) for the adsorption systems in Figures 5 and 6.

	Au_7Cu_{23}/MgO(100)					$Au_{23}Cu_7$/MgO(100)				
Adsorbate	E_{ad}^2 (eV)	r_{O-O} (Å)	$r_{C=O}$ (Å)	Q (e)		E_{ad}^2 (eV)	r_{O-O} (Å)	$r_{C=O}$ (Å)	Q (e)	
				O	CO				O	CO
$CO + O_2$	3.09	1.51	1.18	1.45	0.35	1.64	1.47	1.15	1.18	0.07
CO + O	3.50		1.18	1.21	0.33	1.53		1.15	1.02	0.10
CO + O + O	5.47		1.17	2.21	0.22	2.21		1.16	1.90	0.06

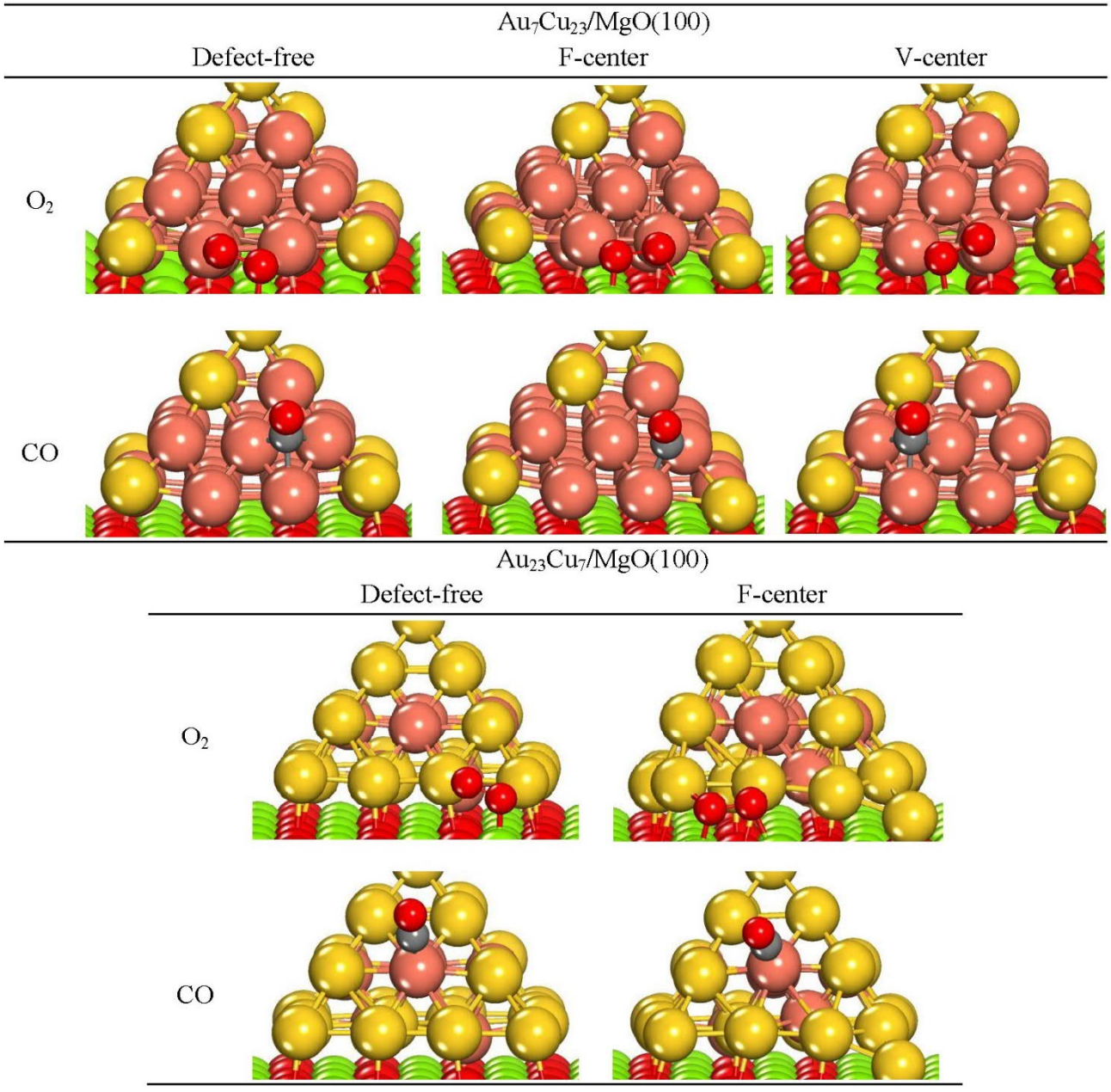

Figure S1 Most stable adsorption configurations of O_2 and CO on Au_7Cu_{23}/MgO(100) and $Au_{23}Cu_7$/MgO(100) with the different supports. Color key: yellow, Au; coral, Cu; green, Mg; red, O; and grey, C.

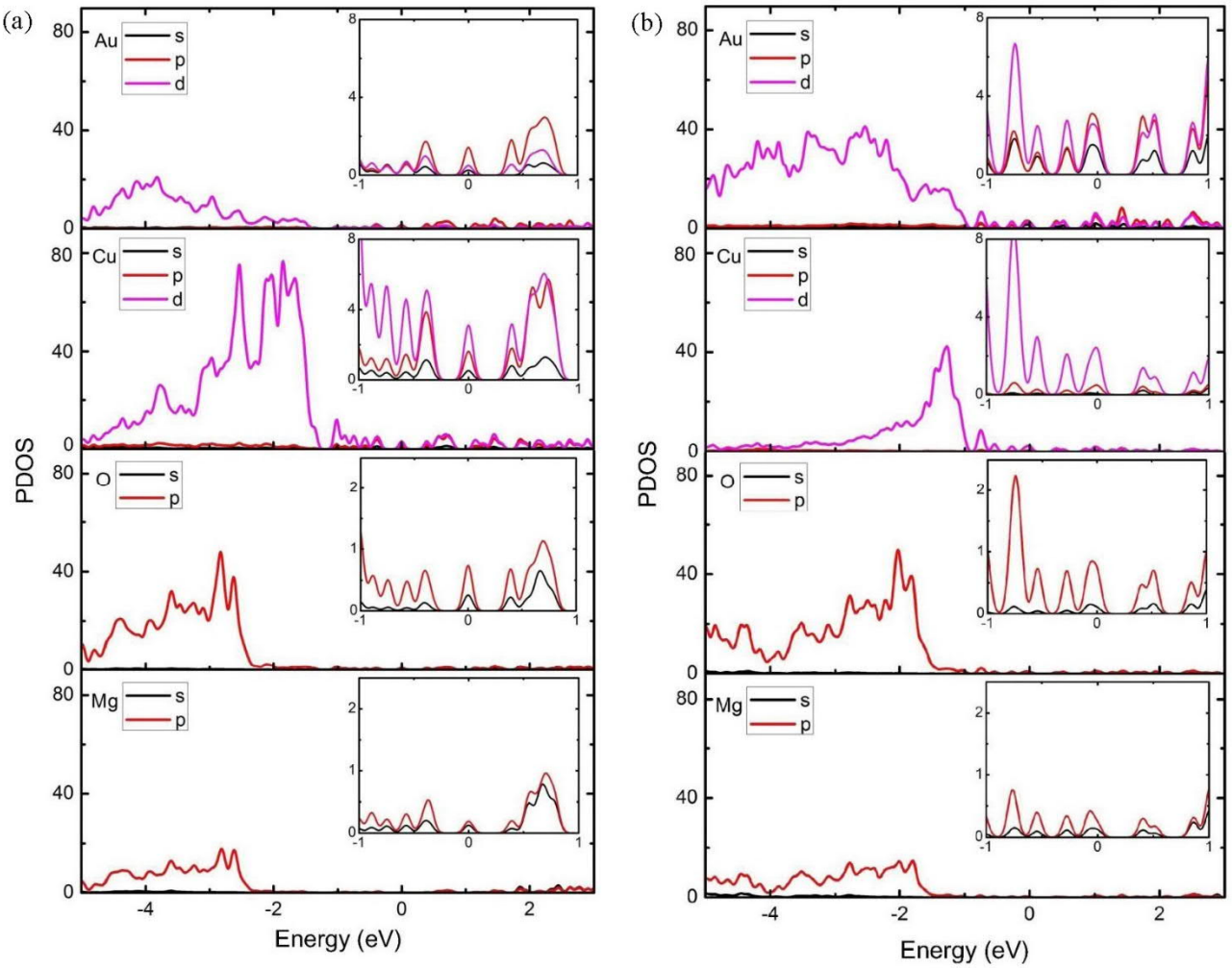

Figure S2 Projected electronic density of states (PDOS) of the (a) Au_7Cu_{23} and (b) $Au_{23}Cu_7$ clusters on the F-center MgO(100) supports and the zoom-in near the Fermi energy in each panel. The PDOS are projected onto the Au and Cu atoms in Au_7Cu_{23} and $Au_{23}Cu_7$ clusters, and Mg and O atoms on the surface layer of MgO(100). The Fermi energy is set at zero.

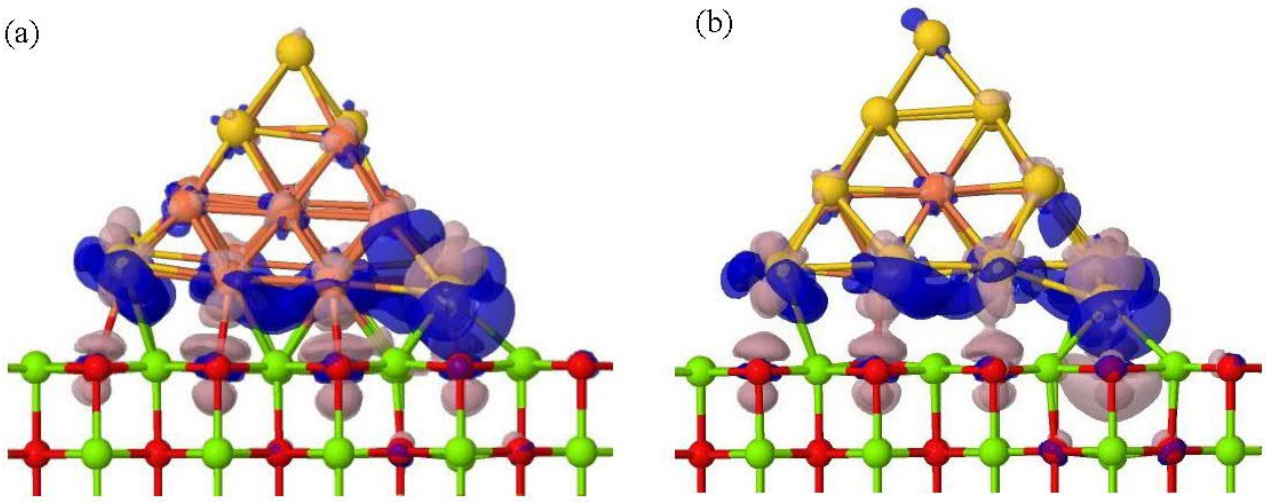

Figure S3 Charge density difference (CDD) of the (a) Au_7Cu_{23} and (b) $Au_{23}Cu_7$ clusters adsorbed on F-center MgO(100) supports. Blue and pink colors represent charge depletion and accumulation, respectively. The isosurface values are ±0.002 e/a_0^3.

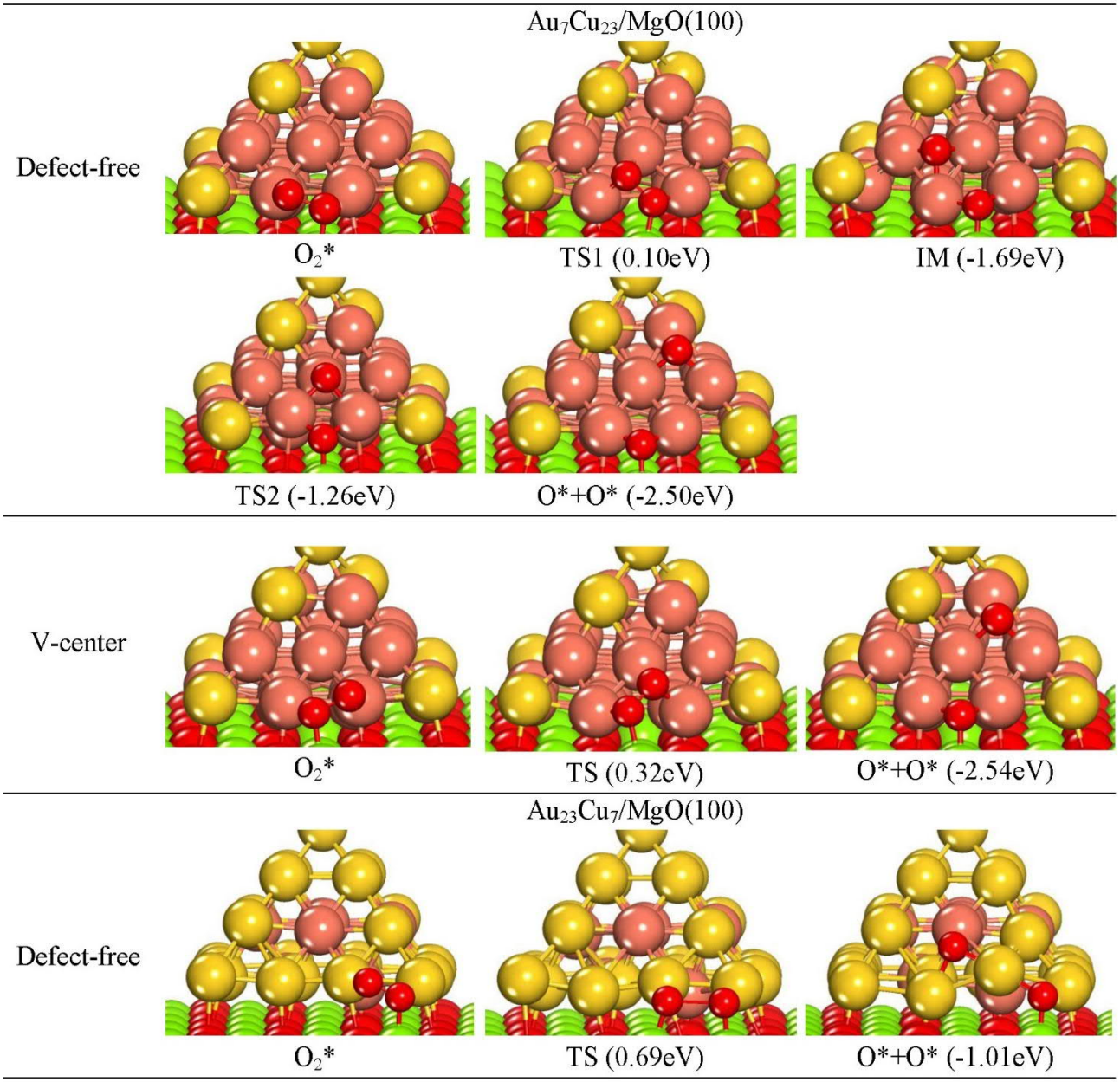

Figure S4 Structures of the initial state (IS), transition state (TS), intermediate state (IM) and final state (FS) of the lowest identified pathways for $O_2 \rightarrow O + O$ on Au_7Cu_{23}/MgO(100) with the defect-free and V-center surfaces, $Au_{23}Cu_7$/MgO(100) with the defect-free surface, and the energy changes with respect to the IS. The symbol '*' refers to the atom or molecule being adsorbed on the cluster.

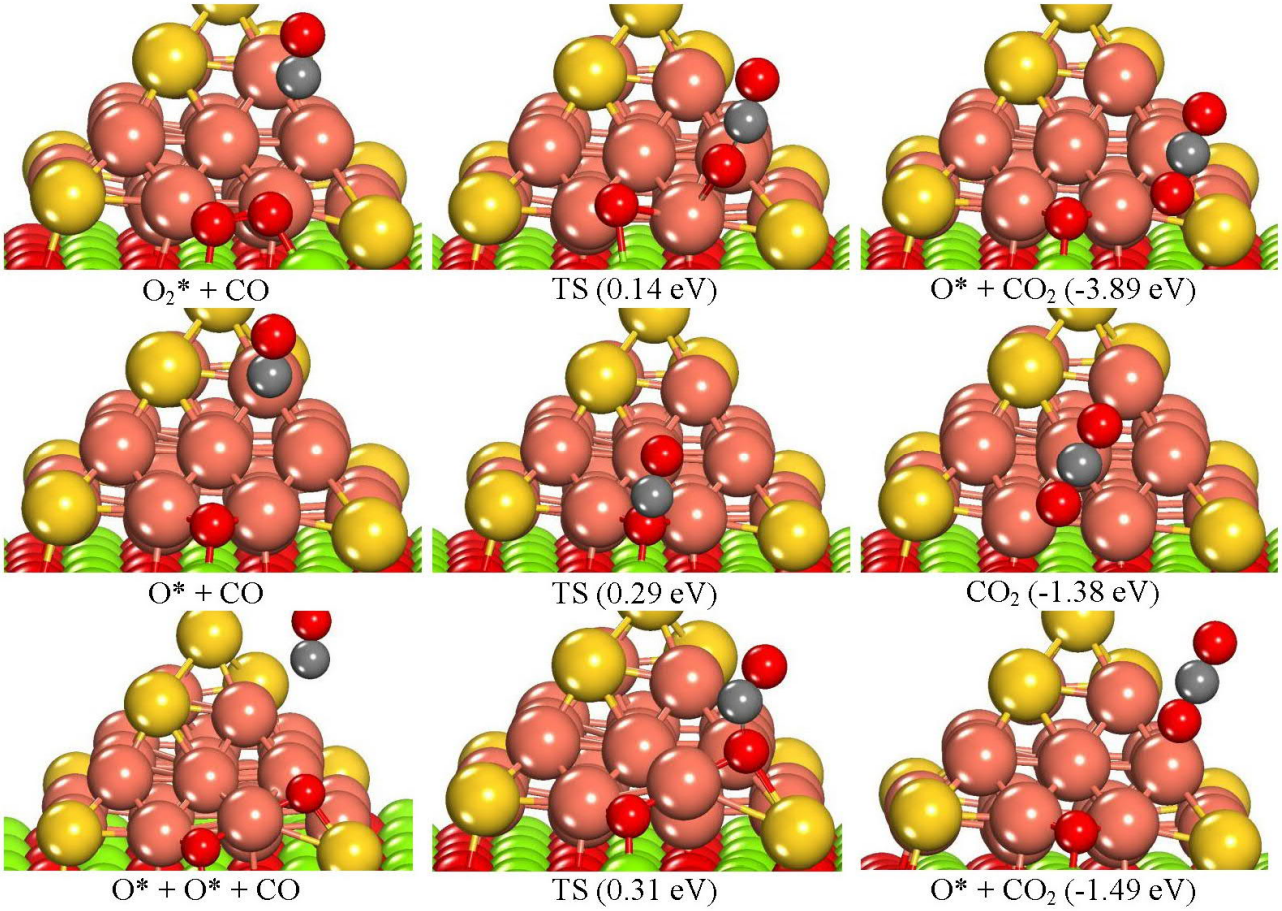

Figure S5 Structures of the initial state (IS), transition state (TS), and final state (FS) for the catalytic CO oxidation on Au_7Cu_{23}/MgO(100) with the F-center surface by Eley–Rideal (ER) mechanism and the energy changes with respect to the IS. The symbol '*' refers to the atom or molecule being adsorbed on the cluster.

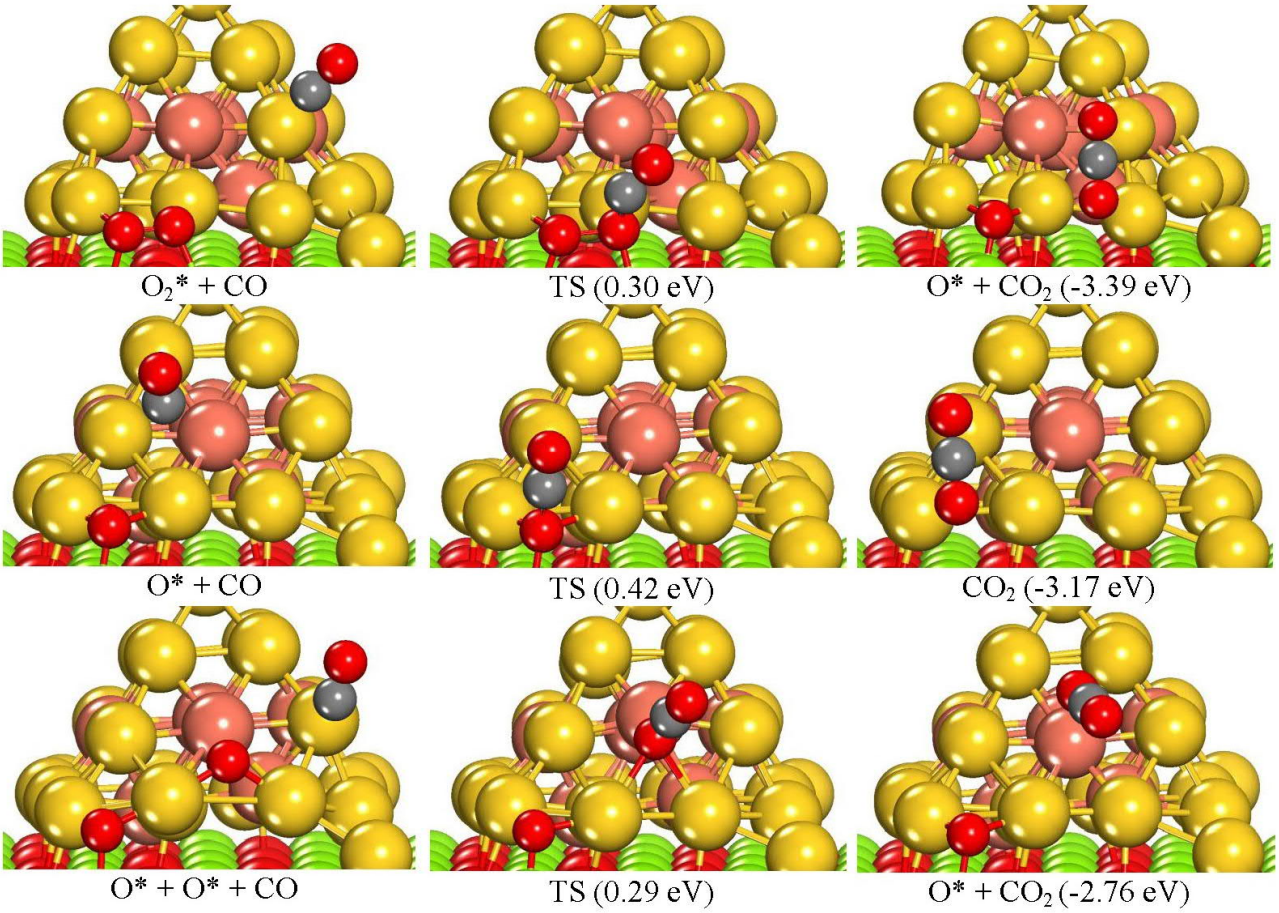

Figure S6 Structures of the initial state (IS), transition state (TS), and final state (FS) for the catalytic CO oxidation on $Au_{23}Cu_7$/MgO(100) with the F-center surface by Eley–Rideal (ER) mechanism and the energy changes with respect to the IS. The symbol '*' refers to the atom or molecule being adsorbed on the cluster.

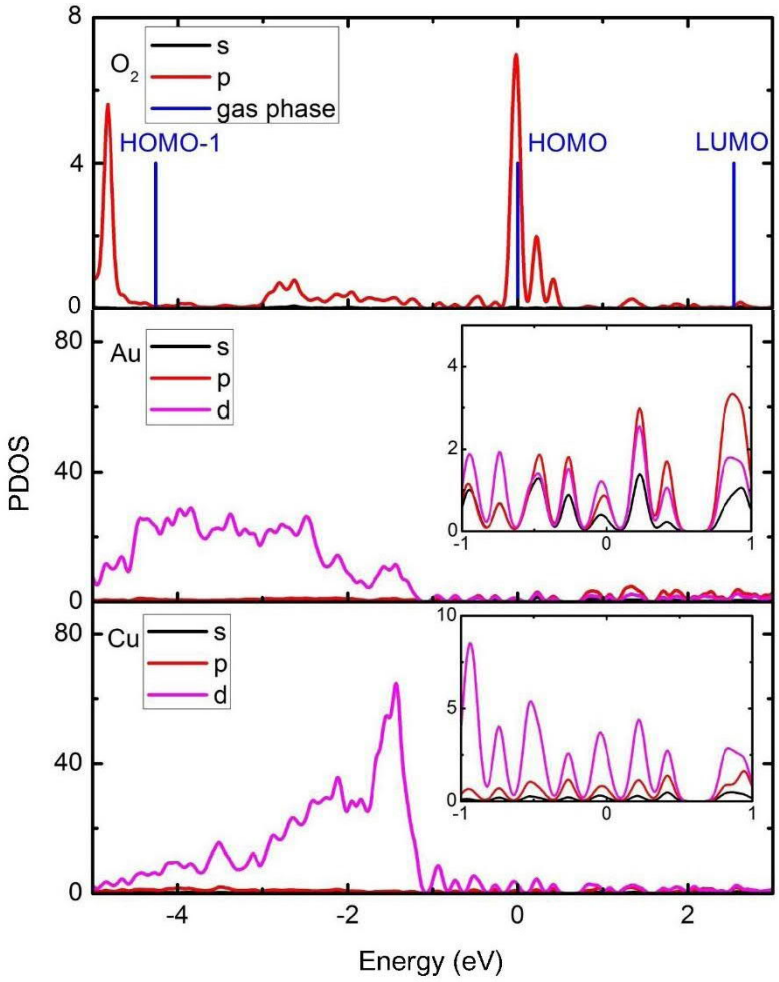

Figure S7 Projected electronic density of states (PDOS) of the O_2 adsorbed $Au_{15}Cu_{15}$ cluster on the F-center MgO(100) support and zoom-ins near the Fermi energy for cluster atoms (insets). HOMO-1, HOMO, and LUMO states of the gas phase triplet O_2 molecule are included for reference in blue color. The PDOS are projected onto the O_2 molecule and Au/Cu atoms in the $Au_{15}Cu_{15}$ cluster. The Fermi energy is set at zero.